Direct Numerical Simulation of catalytic combustion in a meso-scale channel with non-planar walls

Adam M Chabane, Karine Truffin, Christian Angelberger

▶ To cite this version:

HAL Id: hal-02954004

https://ifp.hal.science/hal-02954004

Submitted on 30 Sep 2020

Direct Numerical Simulation of catalytic combustion in a meso-scale channel with non-planar walls

Adam M. Chabane[a], Karine Truffin[a,*], Christian Angelberger[a]

[a]*IFP Energies nouvelles, 1-4 avenue de Bois-Préau, 92852 Rueil-Malmaison, France; Institut Carnot IFPEN Transports Energie*

Abstract

Catalytic combustion of natural gas has a growing interest to improve the flame stability and conversion efficiency in microcombustors. In automotive industry, the improvement of the efficiency of catalytic after-treatment systems are one solution to reduce drastically pollutant emissions. These devices present a honeycomb shape which consists in a grid of millimeter-scale narrow channels whose interior walls are coated with precious metals presenting catalytic properties. Fuels or pollutants are converted through the chemical interactions involving gas-phase molecules and catalytic sites. In order to promote transfers, obstacles can be introduced inside the channels. The numerical simulation is mandatory to help understanding and mastering the underlying phenomena. In the present study, a numerical methodology is proposed to couple surface kinetics and gas phase chemistry with boundary conditions accounting for momentum, heat and mass transfers in order to take into account the interactions between the flow and heterogeneous reactions. Numerical simulations are then performed on the experimental configuration by Dogwiler *et al.* which consists in lean premixed CH_4/air mixture igniting in a *Pt*-coated meso-scale channel with flat walls. The validated numerical methodology is then applied to explore the impact of introducing wall obstacles and segmented coating on the anchoring position of the flame and fuel conversion rate.

Keywords:
Gas-phase ignition, Flame stabilization, Oxidation catalyst, DNS study, Complex geometries

1. Introduction

Catalytic combustion of natural gas has a growing interest to improve the flame stability and conversion efficiency in microcombustors [1]. When combined with catalytically stabilized combustion (CST) it offers gas turbines of power generation systems and other large combustion systems the potential to achieve flame stability and to extend lean flame temperature limit which is conducive to ultra-low NOx emissions [2–4]. Part of the fuel is converted heterogeneously through reactions occurring at the catalytic wall of monoliths where gas-phase molecules and active precious metal sites are involved. The remaining is consumed through homogeneous combustion. In these systems, the presence of a catalytic phase favors reaction paths that would be slow under typical exhaust gas thermodynamic conditions. In automotive industry, exhaust-gas emission control actions can be undertaken through efficient after-treatment devices [5, 6], such as three-way converters for gasoline applications or oxidation catalysts for Diesel applications. These devices present a honeycomb shape which consists in a grid of ceramic or metallic made millimeter-scale narrow channels called monoliths. Interior walls of monoliths are coated with a washcoat over which platinum group metal crystallites exhibiting catalytic properties are distributed.

A review of homogeneous, catalytic and hybrid catalytic-homogeneous microburners is proposed in [7]. The non linear behavior and interactions between surface and gas-phase reactions are presented. The authors also emphazises the lack of understanding of complex coupled mechanisms between flames and walls. Typical reaction rate curves for catalytic systems as a function of temperature are described in [8]. Below 500K, the reaction rate

---

follows an exponential growth which corresponds to a purely kinetic regime i.e, surface reactions do not undergo transfer limitations. At this temperature range, surface reactions are prevailing in the absence of gas-phase ones. For temperatures above 1200K, homogeneous reactions rates are dominating. Under this regime which is referred to as CST [3], catalytic reactions tend to initiate and stabilize homogeneous reactions. Over the temperature range (500K-1200K) homogeneous reactions are activated, however their rates remain low compared to surface ones. The surface reaction rates reach a plateau as a consequence of weak mixing and diffusion that occur near the reactive walls. This results in heat and mass transfer limitations. Therefore, the catalytic conversion rates could be limited by molecular diffusion fluxes and chemical kinetics, which may prove insufficient for certain operating conditions.

In order to enhance transfers under these operating ranges, novel monolith design has been proposed involving transition to turbulence by means of suitable geometric modifications. The enhanced turbulent transport can increase the converter efficiency by up to 30% thus reducing the reactor length and the amount of noble metal catalyst [9, 10]. For this reason several experimental and numerical studies of turbulent hetero-/homogeneous combustion have been conducted in the last years [11–13]. Very recently a new generation of catalytic converters has been developed in which ceramic substrate is segmented into several zones to allow for faster light-off [14]. Another trend has been proposed involving channel wall deformation [15]. These obstacles are created by mechanically deforming the channel wall during the manufacturing process. Different possible wall/obstacle shapes such as baffles, helical/rectangular ribs, sinusoidal/corrugated walls or dimpled tubes and wire coal inserts [16, 17] can therefore be obtained. The contact between the pollutant species carried by the exhaust-gas flow and the catalytic metals at the surface could thereby be enhanced. The resulting flow perturbations, in the form of e.g. recirculation, could lead to higher heat and mass transfer rates to the channel wall and thus larger reaction rates at the surface, which could improve the overall performance of the system. Moreover, the resulting enhancement of transfers and reactivity may enable to reduce the amount of catalytic metals used for coating as the available reactive contact area would be optimized.

Understanding in detail the underlying chemical and physical phenomena inside monolithic channels is a key path to identify potential technological improvements which might concern the obstacles' shape, their numbers and dimensions. Therefore the design of obstacles and the amount of precious metal coating should be explored for an optimized and cost-effective conversion performance [16, 18]. For that purpose, experiments could be carried out but under restricted configurations. Moreover, measurements are limited given the involved confinement and high chemical reactivity [19, 20]. On the contrary numerical simulations allow to explore and design catalytic systems with realistic operating conditions. However experimental data remain necessary in order to validate the numerical modeling. Numerical investigations of the introduction of obstacles or cavities in catalytic meso-scale channels have mostly been reported for applications representative of gas-turbines using CST. Li *et al.* [21, 22] have numerically shown that cavities could enhance the heat and mass transfers inside the cavities, thus resulting in a better conversion of reactants and efficiency in catalytic applications. Also, the low velocity zone within the concave regions have proved to increase flame blow-out limits so that higher energy density operating range could be achieved. One advantage of combining wall cavities with catalytic coating is to avoid gas-phase and surface reactions competition. This behavior is observed in former studies of Di Benedetto *et al.* [23] for planar channels using steady-state modeling. Ran *et al.* [24] have shown numerically that the introduction of one obstacle or a cavity could possibly allow a system downscaling and catalyst loading reduction, as a consequence of a reaction front that anchors closer to the inlet which results in shorter conversion distances. However, it should be stressed that the above mentioned numerical studies mainly focus on steady-state 2D modeling of gas-phase transport. The underlying dynamics yielding the flame to stabilize closer to the inlet is explained through a steady-state analysis which does not provide, to our sense, a full understanding of the flame anchoring process. Moreover, the effect of the presence of multiple obstacles and cavities is not explored. Although full and alternative coating with concave cavity is reported in literature by Li *et al.* using a steady-approach, multi-segmented coating approach applied to obstacles has not been reported to our knowledge. Moreover, a lack of clarity could also be noted regarding the derivation and validation of the boundary conditions used to account for the reactive walls. Regarding automotive catalytic device applications [8, 15, 25], numerical approaches focusing on the introduction of local protuberances in the shape of obstacles are also mostly based on steady-state approaches and assume that the gas-phase chemistry is frozen.

The present study aims at providing a better understanding of the underlying process leading to the steady-state flame stabilization and fuel conversion performance over different catalyst coating and obstacles/cavities configurations using transient numerical investigations which comprise a detailed description of the surface kinetics and the interplay between the gas-phase transport and the reactive wall. In a previous paper [26], the development of boundary

conditions for reactive surfaces was proposed to account for head and mass transfers and it was applied to the simulation of gasification and oxidation of carbonaceous materials with gas-phase combustion under oxy-combustion conditions in a quiescent flow. The aims of the present study is threefold : i/ improve the already existing numerical tool to describe surface reactions on a catalytic wall and account for the interactions between the flow and heterogeneous reactions; ii/ apply the tool to the simulations of reactive flows within millimeter-scale channels with catalytic walls representative of catalytic monoliths; iii/ provide first insight towards the device optimization in terms of conversion performances, by exploring the effect of obstacles and segmented coating on the anchoring positions of the flame and fuel conversion.

This paper is organised as follows. First, a brief recall of the description of the gas-phase governing equations, gaseous and surface kinetics modeling and boundary conditions for momentum, species and energy on reactive interfaces is provided. The reader will refer to [26] for further details. Then emphasis will be given on the numerical resolution method for complex surface kinetics and on the coupling between the gaseous and kinetic solvers. Validation of the overall methodology are herein performed on the experimental configuration by Dogwiler *et al.* [27] which consists of combustion of lean premixed CH_4/air mixture in a *Pt*-coated meso-scale channel with flat walls. Finally, the impact of obstacles on conversion performances are investigated by introducing convex and concave cavities to the planar catalytic channel. The influence of full and segmented *Pt*-distribution is also assessed in order to assist coating optimization strategies.

2. Numerical approach

2.1. Governing flow equations

The AVBP code is used here to describe the physics of gaseous multi-species reactive compressible flows [28]. It solves the compressible Navier-Stokes equations for species mass fractions, momentum and total non-chemical energy using a fully explicit numerical approach. In what follows we assume perfect gas mixtures without buoyancy forces nor volume viscosity effects. Dufour and Soret effects are considered negligible as well as heat transfer by radiation. The validity of these assumptions will be discussed later.

Momentum

$$\frac{\partial \rho \vec{u}}{\partial t} + \vec{\nabla} \cdot (\rho \vec{u} \otimes \vec{u}) = -\vec{\nabla} p + \vec{\nabla} \cdot (\bar{\bar{\tau}}), \tag{1}$$

Gas-phase species

$$\frac{\partial \rho Y_k}{\partial t} + \vec{\nabla} \cdot \left(\rho Y_k \left(\vec{u} + \vec{V}_k \right) \right) = \dot{\omega}_k \qquad \forall k \in \Omega_G, \tag{2}$$

Energy

$$\frac{\partial \rho E}{\partial t} + \vec{\nabla} \cdot (\rho E \vec{u}) = \vec{\nabla} \cdot (-\vec{q}) + \vec{\nabla} \cdot \left(\left(\bar{\bar{\tau}} - p \bar{\bar{\delta}} \right) \cdot \vec{u} \right) + \dot{\omega}_T. \tag{3}$$

E is the total non chemical energy defined as follows [29]:

$$E = \sum_{k \in \Omega_G} h_{s,k} Y_k - (p/\rho) + \frac{1}{2} \sum_{i \in [1, ndim]} u_i^2. \tag{4}$$

The mass density is given by :

$$\rho = \sum_{k \in \Omega_G} (\rho Y_k). \tag{5}$$

The temperature values are computed from E and from the sensible energy look-up table. The thermodynamic static pressure p is given by the equation of state for ideal gas mixture. In Eqs. (1 to 3), $\vec{u}$, u_i, Y_k, $\vec{V}_k$, $\dot{\omega}_k$, $\bar{\bar{\tau}}$, $h_{s,k}$, $\vec{q}$ and $\dot{\omega}_T$ are respectively the flow velocity and its ith component, the mass fraction of species k, its diffusion velocity, the gas-phase species chemical mass rate, the viscous stress tensor, the sensible enthalpy of species k, the diffusive heat flux and the energy rate due to chemical reactions. $\Omega_G = [1, N_g]$ with N_g referring to the total number of gas-phase species in the mixture. The chemical source terms are modeled using the Arrhenius law.

The expression of the heat flux $\vec{q}$ is provided in Eq. (6). It involves the *Fourier* molecular transport and the multi-species sensible enthalpy diffusion. λ stands for the thermal diffusion coefficient and is determined using a

constant Prandtl number P_r as shown in Eq. (7) where C_p is the mass heat capacity of the gas mixture at constant pressure.

$$\vec{q} = -\lambda\vec{\nabla}T + \rho\sum_{k\in\Omega_G} h_{s,k}Y_k\vec{V}_k, \tag{6}$$

$$\lambda = \frac{\mu C_p}{P_r}. \tag{7}$$

The diffusion velocity $\vec{V}_k$ is modeled using the *Hirschfelder and Curtiss* approximation [30] described in Eq. (8). The species diffusion coefficient D_k given in Eq. (10) is determined using the Schmidt number Sc_k which is assumed constant in time and space. μ is the dynamic viscosity of the mixture. In the present study, the Prandtl and Schmidt numbers are set to one. The correction velocity $\vec{V}^{correc}$ defined in Eq. (9) ensures mass conservation.

$$\vec{V}_k = -D_k\frac{\vec{\nabla}X_k}{X_k} + \vec{V}^{correc}, \tag{8}$$

$$\vec{V}^{correc} = \sum_{k\in\Omega_G} D_k\frac{W_k}{W}\vec{\nabla}X_k, \tag{9}$$

$$D_k = \frac{\mu}{\rho Sc_k}, \tag{10}$$

with X_k and W_k respectively the molar fraction and molecular weight of species k and W the mean molecular weight of the gaseous mixture.

2.2. Boundary conditions at the reactive wall

In order to include surface chemistry, the gas-phase problem is coupled with the transport to the gas-surface interface and the reactions. The heterogeneous reactions take place on the surface of the solid following four main steps: 1/ adsorption reactions involving gas-phase and active surface sites, 2/ surface reactions involving adsorbed species and active sites, 3/ desorption reactions, 4/ diffusion of the products into the gas phase. The following assumptions are used in the present study : first, only surface species that stand on the top layer of the reactive support are considered. This means that the bulk species that lie inside the porous network are not accounted for. Second, the local molecular mass diffusion of surface species is considered to be very fast with respect to surface reactions so that the surface species concentration can be assumed as locally homogeneous. This assumption is referred to as the mean field approximation [31].

With respect to these assumptions, the production/consumption of the gas-phase species at the reactive wall via surface reactions are accounted for through the boundary conditions defined in Eqs. (11) to (13) which are applied respectively to the wall-normal velocity, the species mass fraction normal gradient and the wall heat flux. Index w denotes for the gas-phase properties at the wall. $\dot{s}_k$ (kg.m^{-2}.s^{-1}) is the mass production/consumption surface rate of species k. U_{Stefan} is the wall-normal velocity, also called Stefan velocity, which under transient operation is non-zero due to chemical reactions and to the gas-phase species normal gradients that are imposed at the boundary nodes. $\vec{n}$ is the normal to the wall pointing towards the gases. The derivation, validation and numerical implementation of these boundary conditions are detailed in previous studies of Cabrit *et al.* [32, 33] and Chabane *et al.* [26].

$$\vec{u}_w^{BC}\cdot\vec{n} = U_{Stefan} = \frac{1}{\rho_w}\left(\sum_{k\in\Omega_G}\dot{s}_k\right), \tag{11}$$

$$\vec{\nabla}Y_{k,w}^{BC}\cdot\vec{n} = \frac{Y_{k,w}}{D_k\rho_w}\sum_{l\in\Omega_G}\dot{s}_l + \frac{Y_{k,w}}{D_k}\vec{V}_w^{correc}\cdot\vec{n} + Y_{k,w}W_w\left(\sum_{l\in\Omega_G}\frac{1}{W_l}\vec{\nabla}Y_{l,w}\cdot\vec{n}\right) - \frac{\dot{s}_k}{\rho_w D_k}, \tag{12}$$

4

$$
\begin{aligned}
\vec{q}_w^{BC} \cdot \vec{n} = \quad &\underbrace{- \sum_{k \in \Omega_S} h_k \dot{s}_k}_{\substack{\text{Surface heat release} \\ \text{due to surface species}}} \quad \underbrace{- \sum_{k \in \Omega_G} \triangle h_{f,k}^o \dot{s}_k}_{\substack{\text{Surface heat release} \\ \text{due to gas-phase species}}} \quad \underbrace{- \rho_w \sum_{k \in \Omega_G} U_{Stefan} h_{s,k,w} Y_{k,w}}_{\substack{\text{Sensible enthalpy transport} \\ \text{by Stefan flux}}} \\
&\underbrace{- \frac{\dot{m}}{2} \sum_{j \in \mathcal{D}} u_{j,w}^2}_{\text{Kinetic energy}} + \underbrace{(\bar{\bar{\tau}}\vec{u})_{n,w}}_{\text{Viscous heat}} \quad \underbrace{- \lambda^s \vec{\nabla} T_w^s \cdot \vec{n}}_{\substack{\text{heat conduction} \\ \text{in solid wall}}} ,
\end{aligned}
\tag{13}
$$

where Ω_S is the set of surface species involved in surface reactions, h_k is the total enthalpy of species k, $\triangle h_{f,k}^o$ is its standard enthalpy of formation (J.kg^{-1}) and $\dot{m}$ is the normal mass flux at the wall (or Stefan mass flux). The exponent s stands for the solid phase. In the present study, the heat conduction in the wall is neglected. Finally, the evolution equation describing the variation of the surface species site fraction is [34]:

$$
\frac{\partial \theta_k}{\partial t} = \frac{\dot{s}_k}{\Gamma W_k}, \quad \forall \; k \; \in \; \Omega_s.
\tag{14}
$$

θ_k is the site fraction which represents the number of adsorbed molecules on a surface divided by the number of molecules in a filled monolayer on that surface. Γ (mol.m^{-2}) is the site density, i.e. the number of moles of active sites per surface unit of the support. In this paper, Γ is supposed to remain constant.

2.3. Chemical kinetics

Accounting for elementary chemical reactions involved in catalytic combustion is essential in order to capture transient chemical phenomena such as gas-phase ignition and catalytic light-off. In order to simulate the combustion of a lean premixed CH_4 / air mixture the Aramco mechanism (Aramco Mech 1.3) [35] was selected as it describes well the oxidation of methane in lean conditions using 250 species and more than a thousand of reactions. As using such a large scheme in our simulations would yield unpractical CPU times, a reduced skeletal scheme was formulated that would render accurately the chemistry found under the conditions of Dogwiler *et al.* [27].

As combustion of CH_4 is considered, the C1-C2 subset was extracted and reduced using an Error-Propagation based Direct Relation Graph (DRGEP) methodology [36]. The resulting skeletal mechanism, provided as Supplemental material, includes 16 species, 39 bidirectional and 1 unidirectional reactions under the conditions of Dogwiler. 1D flame comparison of the OH concentration predicted with the detailed and the reduced mechanism was performed using PREMIX solver of the CHEMKIN library. The chosen reduction target was a maximal relative deviation of 10% from the predictions by the full mechanism of the average axial OH concentration.

Regarding the catalytic oxidation of methane on platinum, the reaction mechanism of Deutschmann *et al.* [34, 37] is employed. It uses 10 bidirectional and 6 unidirectional reactions with 7 gas-phase and 11 surface species involved. Platinum species (Pt) refers to the catalytic active sites while 10 other surface species represent the ones adsorbed by P_t or resulting from surface-to-surface reactions. The catalyst site density (Γ) is taken equal to 2.72×10^{-5} $mol \cdot m^{-2}$ representative of a polycrystalline platinum surface. The mechanism is provided with the thermochemical data needed to calculate the equilibrium constants and the individual heats of reaction.

2.4. Numerical resolution of the chemistry

As detailed kinetic mechanisms involve a large spectrum of radicals, the implementation of robust and fast solvers for both gas-phase and surface chemical kinetics is required to handle the induced stiffnesses with both an acceptable accuracy and computational cost. Two time integration methods are used in the present study:

- Gas-phase chemistry is solved using a simple explicit 1st order Euler method because the limiting acoustic time step of the compressible explicit CFD simulation is small enough to ensure stability of the time integration method;

- Surface chemistry kinetics is solved using the implicit VODE [38] solver.

Fig. 1 shows a sketch illustrating the solution method for the surface chemistry. Each computational node of the wall mesh is approximated as an independent homogeneous reactor involving surface reactions between gas-phase and surface species. Given N_w wall nodes, a total of N_w independent ODE systems corresponding to a homogeneous reactor and comprising $N_g + N_s + 1$ unknowns is solved. N_g is the number of gaseous species and N_s is the number of surface species. The general form of the ODE system is written as follows:

$$\begin{cases} \vec{\Pi} = \left(\rho Y_{k,w}^{hom}, \theta_k, T_w^{hom} \right), \\ \dfrac{\partial \Pi_k}{\partial t} = R_k^{s,chem}(t) \quad \forall k = [1,..,N_s + N_g + 1]. \end{cases} \tag{15}$$

where $R_k^{s,chem}$ is the chemical operator expressing the rate of change due to surface reactions. In addition to surface sites θ_k, the surface reaction rates depend on the wall temperature T_w and gas-phase species mass fractions adsorbed at the wall $Y_{k,w}$ as well. The temporal variation of T_w and $Y_{k,w}$ is required in the system in order to update their value at every sub-iteration. If the reactive wall is supposed isothermal, the wall temperature does not need to be included thus making the system size equal to $N_g + N_s$ rather than $N_g + N_s + 1$.

3. 2D simulation of catalytic combustion in a meso-scale planar channel

3.1. Experimental configuration and studied cases

The experimental configuration of Dogwiler *et al.* [27] consists of lean premixed methane-air mixtures in a planar channel flow with *Pt* coated interior walls. The reactor is rectangular and consists of two 250 mm long (x-direction) and 100 mm wide (z-direction) ceramic plates that are separated by $H = 7$ mm (in the y-direction). The temperature of the catalytic walls was controlled and monitored in the experiment thanks to a heating/cooling arrangement resulting in longitudinal wall temperature profiles, ranging from 1260 K to 1370 K. The flow is laminar with inlet Reynolds numbers (based on the 7-mm channel height) up to 390. OH-LIF was performed to measure the levels of hydroxyl radical (*OH*) resulting from the gas-phase reactions. For details of the experimental set-up, the reader may refer to [3, 27, 39–42]. Dogwiler *et al.* [27] studied three different cases (labelled in what follows as (a), (b) and (c)) by varying the inlet velocity, temperature and equivalence ratio while the pressure (atmospheric) was kept identical. These conditions are summarized in Table 1.

3.2. Methodology and numerical configuration

3.2.1. Computational domain and boundary conditions

Fig. 2 shows the computational domain. The region colored in red is the region of interest, which corresponds to the part of the channel studied experimentally. Since the experimental channel is more than ten times wider than high, we made the assumption of a 2D domain in the (x,y)-plane. Furthermore, assuming the flow to be symmetric with respect to its half-height, only the lower half of the channel is simulated with the *Pt*-coated planar catalytic wall located at $y = 0$. The justification for this simplifying assumption will be discussed in Section 3.5.

The two blue 2D regions located up- and downstream the domain of interest are added for numerical reasons: the upstream convergent section enables to yield nearly uniform inlet velocity and temperature profiles at the inflow of the domain of interest located at $x = 0$, as in the experiment. The divergent section located downstream the domain of interest is added in order to impose atmospheric pressure at the outflow of the domain of interest.

Table 2 lists the different types of boundary conditions imposed in the computational domain. Inlet and outlet boundary conditions are respectively applied to the convergent entrance ($x = -L_{PI}$) and divergent exit ($x = L_c + L_{PO}$) using the NSCBC method [43, 44]. The temperature (T_{inlet}), species mass fractions ($Y_{CH_4}|_{inlet}$, $Y_{O_2}|_{inlet}$ and $Y_{N_2}|_{inlet}$) and velocity ($\vec{u}|_{inlet}$) are prescribed at the inlet. The velocity imposed at the inlet boundary is calculated in order to reproduce the experimental mass flow rate, i.e, $u_x|_{inlet} \times (h_c/h_{PI})$ is imposed at the convergent entrance. Pressure is the only enforced scalar at the outlet boundary as it remains subsonic. The NSCBC method relaxes the values predicted by the numerical scheme towards the targeted conditions in order to control possible reflections of the waves thus avoiding the propagation of non-physical perturbations.

Prescribed temperatures are numerically imposed on the catalytic wall of the domain of interest for each case using the longitudinal temperature profiles experimentally measured and shown in Fig. 3. The wall temperature profile is

enforced by the means of a conservative relaxation method which relaxes the temperature predicted by the numerical scheme at the wall towards the targeted temperature profile.

The effect of surface reactions on the momentum, mass and heat fluxes at the catalytic wall, is taken into account by correcting the predicted fluxes at the wall using the expressions of Eqs. (11) to (13) with respect to the formulations indicated in Eq. (15). Standard free-slip and adiabatic wall conditions are applied to the walls of the plena. Also, during the non-reactive computations performed to establish the flow, standard impermeable wall conditions are used for the catalytic wall.

3.2.2. Calculation strategy

The convective scheme used in this study is the finite-volume second order in space and time Lax-Wendroff scheme (LW) [45]. Fig. 4 illustrates the calculation strategy followed for the present simulations and comprising the following steps:

- First, the non-reactive steady flow is established by imposing surface and gaseous chemical source terms to zero during a physical time τ_{init} ranging from 0.125 s to 0.25 s, corresponding to one flow-through time. The flow field is initialized using simple homogeneous solutions with the experimental prescribed wall temperatures of the corresponding reactive cases and with oxygen surface site fraction set to one ($\theta_{O(Pt)} = 1$). Therefore the time $t = 0$ refers to the beginning of the reactive simulations starting from a cold flow with established momentum and thermal boundary layers.

- Restarting from the obtained steady chemically inert flow, the computation of reaction source terms is then allowed (except in the plena) and the simulation is run for a physical time $\tau_{reac} = 115$ ms, that is long enough to cover all the phases of the transient combustion described below.

3.2.3. Meshing strategy

The computational domain is discretized using unstructured triangular meshes. Three different sets of meshes are used, all being characterized by a significant coarsening in both plena where reactions are suppressed and coarse meshed helped in dissipating potential numerical perturbations. First, a coarse mesh with typical cell size of 250 μm in both directions is used during the establishment of the non-reactive flow field.

The mesh resolution of the reactive simulations could not be *a priori* set, it was therefore checked *a posteori*. Preliminary studies performed with the CRESLAF solver [46] in two-dimensional reactive channels enabled to define an estimate of the grid resolution. A mesh refinement was then a posteriori performed and showed that convergency of the species profiles were obtained with a cell size of 25 μm (MESH(I)) for the transient phase and 150 μm (MESH(II)) for the steady state. The resulting meshing strategy is summarized in Fig. 5. Mesh (I) exhibits the finest resolution and is used to resolve the stiffest dynamics resulting from the activation of both gas-phase and surface reactions. After a physical time t_{interp} approximately equal to 3 times the ignition time t_{AI}, the gas-phase reaction zone becomes thick enough to require a much coarser mesh, and all flow variables are interpolated to Mesh (II) which is then used during the final stabilization process.

In the following, the auto-ignition time t_{AI} was estimated using heterogeneous reactor simulations with the SENKIN kinetic solver of the CHEMKIN library [47]. It consists of one computational cell, the boundaries of which are all set to be reactive walls, resulting in a simple closed volume reactor exhibiting gas phase and surface reactions, but no molecular or convective transport. The initial conditions were found at the inlet of the channel, except the initial temperature, which was set to the mean channel flow temperature at $t = 0$. t_{AI} refers to the time for which OH reaches 50% of its maximum value and it is equal to 4.62 ms in case (a).

Simulations are performed on OCCIGEN supercomputer from CINES (Bull cluster with a maximum power of 3.5 PFflop/s). The required CPU times for case (a) on MESH (I) and MESH (II) are summarized in Table 3. The acoustic time step (CFL) of the compressible explicit simulations is the limiting time step for all configurations. As a result, a full simulation, using MESH (I), would result in a cost that is estimated to 72 h $\times (12t_{AI}/3t_{AI})$ = 288 h. Such a computation would cost 12 days over 256 processors which is not affordable given the number of simulated cases. This thereby justifies the meshing strategy of the present study. Table 3 also indicates that surface chemistry is twice more expensive in the first phase.

7

3.3. Validation of the steady-state solutions

The steady-state solutions obtained for the 3 simulated cases (a), (b) and (c) are validated by comparing the numerical results with the experimental findings by Dogwiler *et al.* [27]. Figs. 6 to 8 show a comparison between 2D OH-PLIF measurements and the computed 2D maps of OH concentration for the three cases. Similar flame shapes are obtained: the symmetric "V" shapes and the sweep angles are reproduced in an acceptable manner for all cases by the present numerical modeling. The V-flames are due to lower axial velocities at the catalytic wall which results in a penetration of the flame further upstream in the vicinity of the wall.

Correct predictions of the positions where the flames are stabilized and levels of OH concentration are noticed as well. The flame of case (b) stabilizes further downstream and is more stretched because the inlet velocity is two times higher. OH concentration of case (c) presents lower levels than cases (a) and (b) because of a leaner inlet mixture. Also, predicted flame wakes are more spread and exhibit higher OH concentration levels at the flame center than in the experiments.

In order to quantify the axial stabilization of the flames, Table 4 compares the axial distance from the inlet of the catalytic channel and the axial point where the OH concentration reaches its maximum. The relative differences for all cases are smaller than 3%. The normalized error compared with the measurements indicates an order of magnitude equivalent to one channel half-height (h_c) for cases (b) and (c).

Fig. 9 compares the computed axial OH-profiles on the channel plane of symmetry with experimental findings. For all cases, the model overpredicts both the height and the width of the high OH concentration zone. Table 5 quantifies these discrepancies by comparing the relative error in terms of the OH peak value, its axial position L_{OH} and of the width of the high OH zone (defined as the axial distance between two points where OH concentration reaches 25% of the peak value).

Different possible sources of error were investigated in order to explore possible reasons for the differences observed in the OH concentration profiles at the plane of symmetry of the channel:

- Possible uncertainties of wall temperature and inlet conditions do not explain the observed differences between the modeling and the experiment.

- Refining the grid resolution had no impact on the steady-state, confirming *a posteriori* that the reaction front is already well resolved on the coarsest mesh.

- The effect of a third order space and time numerical scheme only had a small impact on the stabilization location (less than 0.1% on case (a)) and OH peak level (less than 2%).

- The choice of the gas-phase chemistry solver (implicit VODE solver or explicit first order Euler method) had no impact on the OH profiles along the plane of symmetry.

- The impact of the radiative heat transfer was *a priori* estimated using the expression given by Barlow *et al.* [48] showing that radiative effects were negligible in these conditions with a maximum contribution of 2% of the total energy (radiative + sensible + chemical) within the reaction zone. However radiation may play a role in heat transfer mechanisms as well as in the location of the initial hot spot zone [49].

- A priori estimations of complex transport on the steady-state using the EGLIB library [50] showed that the approximation made when describing the diffusive transport phenomena was a non negligible cause for discrepancies between the predicted and measured *OH* concentrations. An a priori estimation showed that accounting for complex transport would lead to higher *OH* mass fluxes by diffusion up to a factor 2 at the wall. This is likely to lead to an increase of the quantity of *OH* adsorbed by the catalytic walls, thus decreasing the overall gas-phase *OH* levels. However, it was observed that the Soret and Dufour terms were negligible. Solving the full multicomponent transport system could be very expensive with a high number of species. Moreover, boundary conditions of reactive walls should be derived consistently.

- Last but not least, the reported differences could also be partly attributed to the gas-phase chemical mechanism although results uncertainties related to this reduced mechanism were not quantified.

Considering that the position and shape of the reaction zone is reasonably well reproduced and that the prediction of OH levels is acceptable, the present results can be considered as overall validating the proposed methodology.

3.4. Results concerning the activation of the gas-phase reactions

First, we present results obtained on the phase corresponding to the initialization of gas phase reactions by auto-ignition. This study is performed on case (a) by using the same prescribed wall temperature as boundary condition from Dogwiler at all times (from $t = 0$ to steady state). Chemical reactions are switched on at $t = 0$, leading to an auto-ignition of the reactive mixture.

2D field of the normalized gas-phase heat release rate is provided in Fig. 10a at $\tau = t/t_{AI} = 1.5$, where $t_{AI} = 4.62$ ms in case (a). The reference value $\dot{\omega}_T^{0D}$ is the peak of heat release rate obtained from the heterogeneous reactor computation. It shows that the highest rates of heat release form a kernel downstream. The transition from auto-ignition to a propagating flame is illustrated a few instants later (at $\tau = 1.65$) in Fig. 10b, where the gas-phase heat release presents the shape of a ring.

The time evolutions of OH mass fraction and heat release rate at the location $x = 0.9L_c$ at different instants of the auto-ignition process are shown in Fig. 11. OH mass fraction is normalized by its equilibrium (Y_{OH}^{0D}) value obtained in heterogeneous reactor computation. The overall trend corresponds to the increase with time of both OH mass fraction and gas-phase heat release in the gas-phase and at the wall, as chemical reactions take place in the whole transverse direction. Nevertheless, Fig. 11a shows that the OH transverse profiles present mass fractions that are higher at the wall vicinity. This results from the *OH* desorption from the *Pt* active sites. It is noticed in Fig. 11b that the transverse profiles of the gas-phase heat release rate present similar positive gradients near the wall in the direction normal to the wall and pointing towards the gases. Radical species desorption thereby leads to the promotion of gas-phase reactions. Gaseous chemistry is therefore initially activated in the downstream vicinity of the catalytic plate as surface reactions are activated. In this first phase, methane homogeneous reaction rate is very slow and methane consumption and temperature increase are attributed to catalytic reactions. This is also reported from numerical studies in [49, 51].

Fig. 12 shows the normalized transverse profiles of *OH* mass fraction and heat release at $x = 0.9L_c$ and for different instants ranging from 0.45 t_{AI} to 1.65 t_{AI}. Negative wall gradients computed from the walls and towards the gas of both OH mass fraction and gas-phase heat release are observed. This is because the near-wall OH and gas-phase heat release resulting from the activation of surface reactions progressively diffuse in the upper transverse direction. At 1.65 t_{AI}, both transverse profiles present a difference of 2 orders of magnitude between the wall and the channel center. The elliptical shape of the flame is highlighted by the two dominating peaks in the gas-phase heat release (Fig. 12b).

In order to explain this gap, the characteristic times of gas-phase species diffusion and chemistry are compared by *a priori* estimating the Damköhler number $Da|_{AI} = t_{diff}^{spec}/t_{AI}$ under the conditions taken downstream the channel at $t = 0$. It is defined as the ratio between the ignition time t_{AI} and the characteristic time of species diffusion in the transverse direction ($t_{diff}^{spec} = h_c^2/(\nu S_c)$, with ν the kinematic viscosity of the gas). The resulting $Da|_{AI}$ is of the order of $\simeq 13$. This means that the characteristic time of species diffusion in the transverse direction is much larger than the ignition time of gas-phase reactions.

This could explain why gas-phase chemistry ignites at the channel center regardless of the influence of the catalytic activity at the surface. Similar behaviour is observed in another numerical study [51] using a very simplified one-step gaseous chemistry and aiming at simulating several parallel channels to take into account transverse heat exchanges. Simulation of combustion with deactivated surface reactions, performed under similar conditions, shows that gas-phase reactions are also activated downstream, although the ignition time is slightly higher. This implies that the activation of combustion in such a catalytic channel is governed by the auto-ignition of gas-phase chemistry with a limited perturbative role of surface reactions in the ignition process under the present conditions. It is noteworthy that this mode of homogeneous ignition is different from the one reported in H_2 /air combustion on Pt channels in Brambilla *et al.* [1] where DNS shows that H_2 gaseous ignition is always initiated close to the catalytic wall. It may be related to the different fuel but also to the wall temperature. Indeed conjugate heat transfer simulations are performed in Brambilla leading to a slow heat-up of the solid wall due to the surface heat release. In the present simulation the same high wall temperature profile being imposed as boundary condition from the beginning of the simulation, it may reduce auto-ignition delays in the gaseous phase.

3.5. Comparison with an inert-wall channel

The capacity of catalytic combustion to increase the range of blowout stability compared with homogeneous combustion is discussed in [7]. In the present study, the stabilizing effect of the catalytic walls on gas-phase

combustion is emphasized by numerically deactivating surface reactions. This test is solely performed under the conditions of case (a) using the same prescribed wall temperature. Although non representative of realistic conditions, it allows to evaluate qualitatively the impact of surface reactions on the flame stabilization during the steady-state. In order to capture possible asymmetric features of the flame, the simulations are carried out by considering a full channel without symmetry assumption.

The temporal evolution of the reaction front position (X_f) taken at the flame leading edges, for both inert and reactive wall channels, are plotted in Fig. 13. $X_f = x_{stab}/x^a_{stab}$ is defined as the axial distance between the inlet of the catalytic channel and the axial point where the OH concentration reaches its maximum normalized by the reference anchoring position in case (a). In the inert wall case the value x_{stab} is taken at two transverse positions : $0.5h_c$ and $3.5h_c$. The inert wall case presents an oscillating evolution with a constant amplitude, whereas the temporal evolution of the catalytic case reaches a steady-state.

In order to show the transient behavior of the inert-wall case, OH concentration maps of the inert-wall simulation are shown in Fig. 14 at $23t_{AI}$ and $26t_{AI}$. A slant-shape flame is observed in the vicinity of the channel inlet with a leading edge oscillating between the lower half (Fig. 14b) and the upper half of the channel (Fig. 14c). It is also observed that the reaction front anchors much further upstream when surface reactions are deactivated, i.e, at $x = 0.125L_c$ while the flame stabilizes at the expected location in the catalytic channel, i.e, at $x = 0.34L_c$. The order of magnitude of the difference between the two stabilization locations is 8.5 times the channel total height. As mentionned in Dogwiler attemps, the inert-wall case ignites much farther upstream than the catalytic case because the fuel is not depleted via surface reactions. In the innert channel, the equivalence ratio in front of the propagating flame is $\Phi = 0.36$. In the catalytic channel, the flame is stabilized in region with less fuel ($\Phi = 0.2$) but with higher temperature. Morever the inert wall channel maintains a higher total enthalpy at the ignition location since the contact length to the wall is much shorter. Hence, the inert case forms a stronger flame with higher OH.

Deactivating surface reactions therefore results in an oscillatory asymmetric slant-shape flame that anchors in the vicinity of the inlet, under the present conditions. Although this might lead to shorter conversion distances which is practical for possible system downscaling, instabilities and asymmetries are undesirable as it may lead to reactor safety issues as reported previously [52, 53]. Such behaviors are representative of possible hydrodynamic [54] or thermal-diffusive instabilities [55–57] encountered in laminar meso-scale channels with non-adiabatic walls. The shape and transient behavior observed in the inert case are in line with the experiment of Dogwiler *et al.* [27] although performed under different conditions. Here, the same conditions are adopted for both cases to provide a proper comparison and illustrate numerically that surface reactions restore the symmetric features of flames undergoing asymmetric instabilities as reported in numerical studies of Pizza *et al.* [58]. The investigation of the underlying phenomena of the observed instabilities and the stabilizing effect of surface reactions is out of the scope of this study. Nonetheless, the numerical modeling of the present study shows its capability of reproducing such phenomenological features.

4. Impact of non-planar walls on combustion in a meso-scale channel

4.1. Numerical methodology

4.1.1. Set-up of the simulations

The same strategy is now used to study the potential impact of obstacles and segmented coating on the anchoring positions of the flame and fuel conversion within catalytic meso-scale channels.

To this purpose, the catalytic channel with planar walls is modified by the introduction of cavities and obstacles on the catalytic walls under the conditions of case (a). We stress that simulations are performed here with the same inlet conditions. The prescribed temperature along each vertical wall of each obstacle and cavity is constant and equal to the wall temperature value at the same axial position as in case (a). The aim is to set boundary conditions as close as possible to case (a) in order to perform comparisons and evaluate the impacts of the modified geometries. Transient numerical investigations are thereby performed in order to provide some insight on the underlying process leading to the steady-state flame stabilization and fuel conversion performance.

Figs. 15a and 15b show schematics of the two studied geometries. d/h_c refers to the blocking ratio. The value of 25% was *a posteriori* chosen so that an interaction with the flame could be observed. In order to ensure optimal conversion

rates, the gap to width ratio (referred by g/w) and the ratio w/d are inspired from the study of Li *et al.* [21, 22]. As described in Fig. 16, the obstacles and cavities respectively restrict and increase the channel section by 25%.

Fig. 17 depicts the two types of *Pt*-coating investigated in the present study for both channels with obstacles and cavities:

- Full coating, for which *Pt* covers the whole wall length as shown in Figs. 17a and 17c.

- Segmented coating, for which *Pt* only covers the top edges of obstacles (Fig. 17b), or the edges located between the cavities (Fig. 17d) .

- In OS case, 30% of the channel length of interest is coated, whereas in CS case 66.7% of the upstream half-part of the channel is coated.

Only symmetric channels are considered in the present study in order to save CPU time. Nevertheless, under the conditions of case (a), the symmetry assumption can be justified by the fact that the flame is most probably not sensitive to thermal-diffusive instabilities as reported by Pizza *et al.* [58]. Moreover, as observed in the experiments of Wan *et al.* [59], cavities are likely to maintain the flame symmetry.

4.1.2. Meshing strategy

The transient ignition phase is not of interest as it occurs much further downstream the channel as was explained previously. When the flame comes across the first obstacles or cavities, i.e. at $t \approx 4t_{AI}$, the gas-phase reaction front is considered as sufficiently wide to be resolved with a coarser mesh than MESH (I) described in section 3.2.3. Consequently, a single coarser mesh is used to perform the whole transient simulations with a grid size of 70μm in each direction.

Special care is taken in the present resolution of reactive flows with complex geometries. The stiffest species H within the reaction zone along the channel plane of symmetry is used *a posteriori* to define the grid size. The portion of H mass fraction profile exhibiting values higher than 5% of the peak value is resolved using 250 grid points as shown in Fig. 18. The resulting mesh enables to discretize the obstacles height and the cavities depth with 12 nodes.

4.2. Impact on steady-state solution

4.2.1. Flame anchoring position

Fig. 19 shows a comparison of the *OH* concentration maps for the studied cases with obstacles and cavities. The channel with planar walls is taken as reference.

Significant differences on the flame anchoring position are noticeable. Some explanations are proposed in the following analyses.

- Impact of the obstacles and cavities :

  - (OS) vs (CS): It is observed in Figs. 19b and 19d that for both obstacles and cavities, the segmented coating results in a flame that stabilizes further upstream compared to the planar-wall channel (Fig. 19a). However, the impact of obstacles is more notable compared to that of the cavities.

  - (OF) vs (CF): Figs. 19c and 19e show for both channels with obstacles and cavities that the continuous coating results in a flame that slightly stabilizes further downstream compared to the planar-wall case (Fig. 19a). But the obstacles yield an anchoring position closer to the position of reference compared to the cavities.

- Impact of the *Pt*-coating :

  - (OS) vs (OF): Figs. 19b and 19c indicate that applying a segmented coating to obstacles results in a flame that stabilizes much further upstream compared to the continuous coating.

  - (CS) vs (CF): Similarly, Figs. 19d and 19e show that segmenting the coating in channels with cavities yields a flame anchoring position further upstream compared to the continuous coating. However, the difference between the two types of coating is less pronounced compared to the cases with obstacles ((OS) *vs.* (OF)).

11

Finally, Fig. 19b indicates that the case with obstacles and segmented *Pt*-coating (OS) exhibits the flame anchoring position that is the closest to the inlet.

Longitudinal temperature profiles along the channel plane of symmetry and along the boundary layer are plotted in Fig. 20 for cases OF and CF. The main difference between the configurations with obstacles and cavities is the surface to volume ratio which is 15 % higher in the case OF than in the case CF. As a result, heat transfer between the wall and the gas is intensified in the OF case leading to higher gas temperature values as quantified in Fig. 20 and therefore to a flame that is stabilised slightly upstream. The importance of keeping low value of the pressure drop when designing complex channels is recognized. In the present configurations, the resulting pressure drop in the modified part of the channel is 1.65 Pa in cases with cavities, 3.7 Pa in cases with obstacles to be compared with 1.85 Pa in case (a).

The axial profiles of velocity, temperature and equivalence ratio along the channel plane of symmetry are compared in Fig. 21a for cases OF and OS. For both cases the equivalence ratio decreases progressively due to two simultaneous mechanisms : the oxydation of fuel by both homogeneous combustion and surface reactions. Then an abrupt decrease of the equivalence ratio down to zero is observed together with an increase of the temperature. An intense peak of heat release and OH production are also found in this area (see Fig. 21b) which are characteristic of propagating flame. In case OF, values of the laminar flame speed obtained from 1D computations at the local temperature and composition conditions are indicated in Fig. 21a. Two observations are noticeable. First there is a very high sensitivity of the laminar flame speed to the variations of the local conditions. Second, just upstream the flame front, the laminar flame speed is quite close to the local gas velocity. This confirms that the propagating front is stabilized in the center of the channel at a position where its laminar flame speed reaches the opposite value of the flow velocity in the fresh gas side.

Coming back to the OS case (red dashed lines in Fig. 21a), it can be seen that the equivalence ratio decreases slower than in the OF case. This difference is due to the catalytic surface which is smaller in OS case, therefore leading to a higher level of methane in the gas flow: the consumption rate of methane on the catalytic wall is 9.935 μg/s in OS case while it is 14.8 μg/s in OF case.

A singular phenomena is observed on OS and CS cases with the presence of gas-phase heat release spots in the cavity or between two obstacles just upstream of the main reaction zone. The heat release and the velocity vectors near the wall in case OS are visualised in Fig. 22a. It is showed that this reaction spot is convected away from the wall at the leading edge of the obstacle towards the main flame front. This reaction zone leads to the formation of species like CH_2O and CH_3 and to an increase of the gas temperature near the wall and above the obstacles as seen in Fig. 22b. The positions of the obstacles are indicated with grey bars. Although there is no clear interplay between both reaction fronts, this hot zone may favor the stabilisation of the propagating flame.

The observed differences are finally quantified in Table 6 by comparing the positions at which the flames are stabilized normalized by the channel length and half-height. Further analysis is provided in the next sections to give more insights on the stabilization mecanims. Noticeably, the channel with obstacles and segmented coating (OS) allows the flame to stabilize at a position that is $3 \times h_c$ closer to the inlet compared to the anchoring position for the planar-wall case. The same type of *Pt*-loading applied to the channel with cavities (CS) has a similar impact but is less pronounced. Compared to the planar-wall case, the CF case exhibits a flame that anchors one channel half-height further from the inlet whereas the impact of cavities and full coating (OF) is negligible.

The effect is moderate under the present conditions ($|x_{stab} - x_{stab}^{ref}|/L_c < 5\%$) but a significant impact could possibly be expected for a further optimized obstacle geometry or coating. The observations indicate that coating only the interior walls in a segmented manner allows the flame to stabilize further upstream. These findings could indicate that an OS solution could lead to more compact designs for catalytic converters, the anchoring of the flame closer to the inlet requiring a shorter coated section as compared to the one for the planar or cavity cases.

4.2.2. Fuel conversion rates

We define here the methane conversion, referred in what follows as MC :

$$MC = 100 \times \left(Y_{CH_4}|_{inlet} - \bar{Y}_{CH_4}(x) \right) / Y_{CH_4}|_{inlet} \tag{16}$$

$\bar{Y}_{CH_4}$ is the average methane mass fraction integrated along the channel height. The conversion distance is defined as the distance between the channel inlet and the position in the channel where MC = 100. Fig. 23 shows the MC

profiles. The red lines indicate where the corners of the obstacles and cavities are located. The observations are listed as follows :

- Fig. 23a shows in $0 \leq x \leq 0.26L_c$ that the MC of both types of *Pt*-coating over obstacles is lower compared to the planar-wall channel before reaching the flame. At this part of the channel, the segmented coating particularly exhibits the lowest MC values. Notably, the MC of both OS and OF cases increases over the top edge of the obstacles as the obstacle corners are reached.

- Fig. 23b shows in $0 \leq x \leq 0.26L_c$ that the MC of both types of *Pt*-coating decreases as the cavity corners are reached. This decrease results in a slightly lower MC values inside the cavities compared to the planar-wall channel. The MC then increases outside of the cavities. The difference between the two types of coating is however less pronounced compared to the channel with obstacles.

- The segmented coating enables a shorter conversion distance than the full coating for both channels with obstacles and cavities.

The above observations could be explained as follows :

- Full *Pt* coating presents a more important catalytic surface than the segmented one which yields higher methane consumption through surface adsorption by the *Pt* active sites. This explains why the MC is higher in $0 \leq x \leq 0.26L_c$ if a continuous coating is applied, especially for the cases with obstacles (Fig. 23a). The difference between the two types of coating is less notable for the cases with cavities (Fig. 23b) because the coating ratio is smaller in the OS case compared to CS case.

- The shorter conversion distances resulting from the segmented coating is explained by the fact that the flame stabilizes further upstream as shown in Fig. 19. As gas-phase reactions govern fuel consumption near the flame, conversion rates are likely to be shorter for the OS and CS cases for which the flame stabilizes closer to the inlet.

- Regarding the channels with obstacles (OF and OS), the increase near the obstacle corners could be explained by the fact the channel section is restricted which yields a shorter diffusive distance between the bulk fuel and the catalyst. This leads to higher mass transfer to the reactive top edge of the obstacle. In contrast, CS and CF cases exhibit decreasing MC near the cavities because of a higher diffusive distance. The resulting wall mass transfers are lower.

To summarize, the decrease of the gap size by the presence of obstacles increases both mass and heat transfer rates by diffusion and by convection. Increasing heat transfer rates is desirable for faster methane conversion by stabilizing homogeneous combustion upstream. The full coating in the pre-heat zone is detrimental to the methane conversion due to an overly lean fuel/air mixture.

4.3. Impact on flame transients

In order to complete the analysis, the effect of obstacles and segmented coating on transient dynamics of the flame propagation is subsequently studied. The study is focusing here on OS and OF cases, as a similar behavior has been observed with cavities.

Fig. 24 shows the overall temporal evolution of the normalized flame front position for the cases with obstacles. Noticeably, the introduction of obstacles results in a propagation speed of the gas-phase reaction front that is slower compared to the planar channel, especially in the case of continuous coating (OF). In particular, the reaction front in the partially coated cases (OS) undergoes a sequence of abrupt variations starting from $\tau \approx 4$. At $\tau \approx 7.5$, the flame position of the OS case sharply decreases to anchor closer to the inlet compared to the planar channel and the OF case, as was shown in Fig. 19. The OF case reaction front propagates smoothly and stabilizes at a channel position similar to the planar wall case.

In order to understand these time evolutions, the transient history of the gas-phase heat release maps and the channel plane of symmetry profiles of the OH mass fraction are described in what follows.

13

4.3.1. Segmented Pt-coating (OS)

Fig. 25 shows for the OS case the transient history of the gaseous heat release maps and the OH mass fraction axial profiles at the channel plane of symmetry. At $7t_{AI}$, Fig. 25a (left) shows that the heat release spot located in the cavity yields a reaction front. Therefore, two reaction fronts are observed which consist in the propagating V-flame located downstream the channel and the one emerging from the cavity located in the left side of the V-flame. The formation of a new reaction front inside the cavity coincides with a small increase in the OH mass fraction at $x = 0.3L_c$ as shown by Fig. 25a (right). A decrease of the V-flame sweep angles is observed at $\tau = 7.2$ (Fig. 25b (left)). In the meantime, the reaction front emerging form the cavity comes across the V-flame as it propagates in the transverse direction. This yields a formation of a small OH peak at the channel plane of symmetry ($x = 0.3L_c$), as shown in Fig. 25b (right). As the two reaction fronts come across each other, Fig. 25c (left) indicates at $7.5t_{AI}$ that the reaction front which is emerging from the cavity results in a V-flame, whereas the tails of the V-flame that are initially propagating upstream the channel form a small kernel of fresh gases characterized by the trough (off-peak) in the OH profile on the plane of symmetry for $0.31 \leq x \leq 0.32$ (Fig. 25c (right)). Finally, Fig. 25d (left) shows at $\tau = 7.75$ that the initial flame undergoes complete extinction while the V-flame that was formed in the cavity propagates upstream as represented by the upstream convection of the OH peak shown in Fig. 25d (right). From these observations, the following scenario can be proposed for the flame/obstacles interaction in the context of segmented coating : As the V-flame propagates upstream the channel, the closest cavity could be preheated through heat diffusion which yields an ignition spot inside the cavity. This results in a reaction front that evolves into a V-flame which consumes the incoming fresh gases. Consequently, the initial forefront of combustion undergoes extinction. The flame does not propagate in a standard manner as in the planar-wall case: the dynamics corresponds to a sequence of flames resulting from the evolution of auto-ignition spots which might favor a further upstream propagation of the flame. The flame stabilizes when the local conditions are no longer promoting auto-ignition and the propagation of the resulting secondary front. It is stressed that the abrupt decrease of the X_f profiles shown in Fig. 24 are now explained by the reaction front emerging from the cavities.

4.3.2. Full Pt-coating

Fig. 26(left) shows for the OF case the transient history of the gaseous heat release maps. At $\tau = 9.85$ (Fig. 26a), the gas-phase heat release spot in the first cavity corner is considerably less pronounced compared to the OS case (Fig. 25) as the V-flame propagates upstream. At $\tau = 10.2$, the near-wall tails of the flame are extended towards the cavity (Fig. 26b). Temporal evolutions of OH mass fraction profiles at the channel plane of symmetry in Fig. 26c shows that the OH peak remains at the same level but progresses upstream. The heat release presents lower amplitudes than the segmented case. This could be explained by the fact that the level of adsorbed OH is much higher than the levels of the segmented case, which yields lower gas-phase activity.

In a similar way as previously mentioned, the following scenario can be proposed for the flame/obstacles interaction in the context of full coating : In the case of channels with full *Pt*-coating, the chemical activity is smoothed out over the whole channel compared to the segmented catalyst. This results in conditions that are less favorable for the formation of auto-ignition spots in the cavities. The flame is therefore less likely to propagate further upstream. This explains why fully *Pt*-coated catalysts present flame anchoring positions that are located further downstream thus resulting in a longer fuel conversion distance.

5. Conclusions

In this paper, 2D simulations of gas-phase combustion of a lean premixed CH_4/air mixture in a catalytic meso-scale channel with planar walls are presented. First, the results are validated at steady-state by comparing the numerical results with experimental data of Dogwiler *et al.* [27]. Second some insight is provided into the ignition and flame propagation processes within catalytic channels. Finally, deactivating surface reactions enables to emphasize the stabilizing effect of the catalytic walls on gas-phase combustion. The main conclusions are listed as follows :

- The comparisons of the steady-state results (Section 3.3) with the experiments [27] reveals that the present numerical modeling is capable of reproducing the main features of the flames under different inlet conditions: The V-shaped flames and the sweep angles are reproduced with an acceptable manner. Comparable predictions of the flame anchoring position and levels of OH concentration are obtained as well.

- The transient analysis (Section 3.4) allows to show that the flame is initiated at the channel rear. Surface reactions are found to impact marginally gas-phase auto-ignition.

- Deactivating surface reactions (Section 3.5) results in an oscillatory asymmetric slant-shape flame that anchors much further upstream compared to the catalytic channel which is also observed in the experiments of Dogwiler *et al.* [27]. The numerical modeling of the present study has thereby shown its *a priori* ability of reproducing the possible instabilities encountered in meso-scale channels with inert walls and the stabilizing effects of surface reactions.

Despite the observed discrepancies with the experimental findings of Dogwiler [27], the present modeling has shown its capability of capturing the main features of the flame within catalytic meso-scale channels with planar walls. These observations enable to validate the modeling and resolution of both gas-phase and surface kinetics on the one hand, and the use of boundary conditions to represent the interplay between the gas-phase transport and the reactive wall on the other hand.

Four different wall configurations are explored, combining either obstacles or cavities, and a continuous or segmented Pt-coating. The analysis of these simulations indicates that the combination of obstacles with a segmented coating allows achieving the increase of methane conversion rate, as the flame anchors further upstream compared to the one of the initial planar channel. Quantitative analysis shows that the benefit predicted for selectively coated obstacles is explained by a specific transient flame dynamics resulting from successive auto-ignitions in the cavities between obstacles. This dynamics allows the flame to propagate further upstream than with planar walls despite the higher flow velocities due to the local flow section restrictions induced by the obstacles. The analysis reveals also that the flame anchoring position is piloted by local flow conditions. The optimized configuration for fast methane conversion is obtained through enhanced thermal transfer using obstacles and segmented catalytic walls which at the same time stabilize the flame and enable flame propagation towards the inlet.

These findings can be considered to open fruitful perspectives for contributing to the optimization of the design of catalytic combustors using the present modeling approach. Especially, combining obstacles with segmented coating would allow a more efficient and thus less costly usage of Pt-coating as a consequence of intensified interactions between the gas flow, gas phase chemistry and surface chemistry.

References

[1] A. Brambilla, C. E. Frouzakis, J. Mantzaras, A. Tomboulides, S. Kerkemeier, K. Boulouchos, Detailed transient numerical simulation of h2/air hetero-/homogeneous combustion in platinum-coated channels with conjugate heat transfer, Combust. Flame 161 (10) (2014) 2692–2707.

[2] R. Sui, W. Liang, J. Mantzaras, C. K. Law, Coupled reaction mechanism reduction for the hetero-/homogeneous combustion of syngas over platinum, Combust.Flame 214 (2020) 37 – 46.

[3] M. Reinke, J. Mantzaras, R. Bombach, S. Schenker, A. Inauen, Gas phase chemistry in catalytic combustion of methane/air mixtures over platinum at pressures of 1 to 16 bar, Combust. Flame 141 (4) (2005) 448–468.

[4] R. Carroni, V. Schmidt, T. Griffin, Catalytic combustion for power generation, Catalysis Today 75 (1) (2002) 287 – 295, environmental Catalysis:a step forward.

[5] P. Granger, V. I. Parvulescu, Catalytic nox abatement systems for mobile sources: from three-way to lean burn after-treatment technologies, Chemical Reviews 111 (5) (2011) 3155–3207.

[6] A. Russell, W. S. Epling, Diesel oxidation catalysts, Catalysis Reviews 53 (4) (2011) 337–423.

[7] N. S. Kaisare, D. G. Vlachos, A review on microcombustion: Fundamentals, devices and applications, Prog. Energy and Combust. Sci. 38 (3) (2012) 321 – 359.

[8] M. F. Zwinkels, S. G. Järs, P. G. Menon, T. A. Griffin, Catalytic materials for high-temperature combustion, Catalysis Reviews–Sci. and Eng. 35 (3) (1993) 319–358.

[9] H. Santos, M. Costa, Modelling transport phenomena and chemical reactions in automotive three-way catalytic converters, Chemical Eng. J. 148 (1) (2009) 173 – 183.

[10] M. Kumar, M. Bhandwal, M. Sharma, A. Verma, U. Srivastava, R. K. Tyagi, Effect of creating turbulence on the performance of catalytic converter, Int. J. Performability Eng. 12 (2) (2016) 115–120.

[11] C. Appel, J. Mantzaras, R. Schaeren, R. Bombach, A. Inauen, Turbulent catalytically stabilized combustion of hydrogen/air mixtures in entry channel flows, Combust. Flame 140 (1) (2005) 70 – 92.

[12] B. O. Arani, C. E. Frouzakis, J. Mantzaras, F. Lucci, K. Boulouchos, Direct numerical simulation of turbulent channel-flow catalytic combustion: Effects of reynolds number and catalytic reactivity, Combust. Flame 187 (2018) 52 – 66.

[13] B. O. Arani, C. E. Frouzakis, J. Mantzaras, K. Boulouchos, Direct numerical simulations of turbulent catalytic and gas-phase combustion of h2/air over pt at practically-relevant reynolds numbers, Proc. Combust. Inst. 37 (4) (2019) 5489 – 5497.

[14] H. A. Ibrahim, W. H. Ahmed, S. Abdou, V. Blagojevic, Experimental and numerical investigations of flow through catalytic converters, Int. J. Heat Mass Transfer 127 (2018) 546 – 560.

[15] S. L. Andersson, N. H. Schoeoen, Methods to increase the efficiency of a metallic monolithic catalyst, Indust. & Eng. Chem. Research 32 (6) (1993) 1081–1086.

[16] A. M. Holmgren, Enhanced mass transfer in monolith catalysts with bumps on the channel walls, Indust. & Eng. Chem. Research 38 (5) (1999) 2091–2097.

[17] L. L. Raja, R. J. Kee, L. R. Petzold, Simulation of the transient, compressible, gas-dynamic behavior of catalytic-combustion ignition in stagnation flows, Symp. (Int.) on Combust. 27 (2) (1998) 2249 – 2257.

[18] K. Ramanathan, V. Balakotaiah, D. H. West, Geometry effects on ignition in catalytic monoliths, AIChE journal 50 (7) (2004) 1493–1509.

[19] J. Mantzaras, Progress in non-intrusive laser-based measurements of gas-phase thermoscalars and supporting modeling near catalytic interfaces, Prog. Energy Combust. Sci. 70 (2019) 169 – 211.

[20] S. B. Rasmussen, M. A. Bañares, P. Bazin, J. Due-Hansen, P. Ávila, M. Daturi, Monitoring catalysts at work in their final form: spectroscopic investigations on a monolithic catalyst, Phys. Chem. Chem. Phys. 14 (7) (2012) 2171–2177.

[21] Y.-H. Li, G.-B. Chen, F.-H. Wu, T.-S. Cheng, Y.-C. Chao, Effects of catalyst segmentation with cavities on combustion enhancement of blended fuels in a micro channel, Combust. Flame 159 (4) (2012) 1644–1651.

[22] Y.-H. Li, G.-B. Chen, H.-W. Hsu, Y.-C. Chao, Enhancement of methane combustion in microchannels: effects of catalyst segmentation and cavities, Chem. Eng. J. 160 (2) (2010) 715–722.

[23] A. Di Benedetto, G. Landi, V. Di Sarli, P. Barbato, R. Pirone, G. Russo, Methane catalytic combustion under pressure, Catalysis Today 197 (1) (2012) 206–213.

[24] J. Ran, L. Li, X. Du, R. Wang, W. Pan, W. Tang, Numerical investigations on characteristics of methane catalytic combustion in micro-channels with a concave or convex wall cavity, Energy Conversion Manag. 97 (2015) 188–195.

[25] K. W. Aniolek, A CFD study of diesel substrate channels with differing wall geometries, SAE Technical Paper (2004) 2004–01–0152.

[26] A. M. Chabane, K. Truffin, A. Nicolle, F. Nicoud, O. Cabrit, C. Angelberger, Direct numerical simulation of combustion near a carbonaceous surface in a quiescent flow, Int. J. Heat Mass Transfer 84 (2015) 130–148.

[27] U. Dogwiler, J. Mantzaras, P. Benz, B. Kaeppeli, R. Bombach, A. Arnold, Homogeneous ignition of methane-air mixtures over platinum: Comparison of measurements and detailed numerical predictions, in: Symp. (Int.) on Combust., Vol. 27, Elsevier, 1998, pp. 2275–2282.

[28] T. Schoenfeld, The avbp handbook, http://www.cerfacs.fr/4-26334-The-AVBP-code.php (2008).

[29] T. Poinsot, D. Veynante, Theoretical and numerical combustion, RT Edwards, Inc., 2005.

[30] J. O. Hirschfelder, C. F. Curtiss, R. B. Bird, et al., Molecular theory of gases and liquids, Vol. 26, Wiley New York, 1954.

[31] O. Deutschmann, Interactions between transport and chemistry in catalytic reactors, Habilitation thesis, Ruprecht-Karls-Universität Heidelberg, 2001.

[32] O. Cabrit, Wall modeling of the flow inside solid rocket motor nozzles, Ph.D. thesis, Montpellier 2 (2009).

[33] O. Cabrit, F. Nicoud, Direct numerical simulation of a reacting turbulent channel flow with thermochemical ablation, J. Turbulence 11 (44) (2010) 1–33.

[34] O. Deutschmann, R. Schmidt, F. Behrendt, J. Warnat, Numerical modeling of catalytic ignition, in: Symp. (Int.) Combust., Vol. 26, Elsevier, 1996, pp. 1747–1754.

[35] W. K. Metcalfe, S. M. Burke, S. S. Ahmed, H. J. Curran, A hierarchical and comparative kinetic modeling study of c1- c2 hydrocarbon and oxygenated fuels, Int. J. Chem. Kinetics 45 (10) (2013) 638–675.

[36] P. Pepiot-Desjardins, H. Pitsch, An efficient error-propagation-based reduction method for large chemical kinetic mechanisms, Combust. Flame 154 (1) (2008) 67–81.

[37] http://www.detchem.com/mechanisms/sm_Pt_CH4_O2_1.2_CHEMKIN (1996).

[38] P. N. Brown, G. D. Byrne, A. C. Hindmarsh, Vode: A variable-coefficient ode solver, SIAM J. Sci. Stat. Comput. 10 (5) (1989) 1038–1051.

[39] J. Mantzaras, New directions in advanced modeling and in situ measurements near reacting surfaces, Flow, Turb. Combus. 90 (4) (2013) 681–707.

[40] X. Zheng, M. Schultze, J. Mantzaras, R. Bombach, Effects of hydrogen addition on the catalytic oxidation of carbon monoxide over platinum at power generation relevant temperatures, Proc. Combust. Inst. 34 (2) (2013) 3343 – 3350.

[41] X. Zheng, J. Mantzaras, R. Bombach, Hetero-/homogeneous combustion of ethane/air mixtures over platinum at pressures up to 14bar, Proc. Combust. Inst. 34 (2) (2013) 2279–2287.

[42] A. Brambilla, M. Schultze, C. E. Frouzakis, J. Mantzaras, R. Bombach, K. Boulouchos, An experimental and numerical investigation of premixed syngas combustion dynamics in mesoscale channels with controlled wall temperature profiles, Proc. Combust. Inst. 35 (3) (2015) 3429–3437.

[43] F. N. L. Selle, T. Poinsot, Actual impedance of nonreflecting boundary conditions: Implications for computation of resonators, AIAA J. 42 (5) (2007) 958 – 964.

[44] D. H. Rudy, J. C. Strikwerda, A nonreflecting outflow boundary condition for subsonic navier-stokes calculations, J. Comput. Phys. 36 (1) (1980) 55 – 70.

[45] F. Tagliante, T. Poinsot, L. M. Pickett, P. Pepiot, L.-M. Malbec, G. Bruneaux, C. Angelberger, A conceptual model of the flame stabilization mechanisms for a lifted diesel-type flame based on direct numerical simulation and experiments, Combust. Flame 201 (2019) 65 – 77.

[46] M. E. Coltrin, H. Moffat, R. Kee, F. Rupley, Creslaf (version 4. 0): A fortran program for modeling laminar, chemically reacting, boundary-layer flow in cylindrical or planar channels, Tech. rep., Sandia National Labs., Albuquerque, NM and Livermore, CA (United

States) (1993).

[47] R. Kee, F. Rupley, J. Miller, M. Coltrin, J. Grcar, E. Meeks, et al., Theory manual chemkin release 4.0. 1, reaction design (2004).

[48] R. S. Barlow, A. N. Karpetis, J. H. Frank, J.-Y. Chen, Scalar profiles and no formation in laminar opposed-flow partially premixed methane/air flames, Combust. Flame 127 (3) (2001) 2102 – 2118.

[49] S. Karagiannidis, J. Mantzaras, Numerical investigation on the start-up of methane-fueled catalytic microreactors, Combustion and Flame 157 (7) (2010) 1400 – 1413. doi:https://doi.org/10.1016/j.combustflame.2010.01.008.

[50] A. Ern, V. Giovangigli, Eglib: A general-purpose fortran library for multicomponent transport property evaluation, Manual of EGlib version 3 (2004) 12.

[51] G. Landi, A. Di Benedetto, P. S. Barbato, G. Russo, V. Di Sarli, Transient behavior of structured lamno3 catalyst during methane combustion at high pressure, Chem. Eng. Sci. 116 (2014) 350–358.

[52] G. A. Viswanathan, M. Sheintuch, D. Luss, Transversal hot zones formation in catalytic packed-bed reactors, Industrial & Eng. Chem. Research 47 (20) (2008) 7509–7523.

[53] B. Veyssière, M. Arrigoni, S. Kerampran, Influence of mixture composition on the oscillatory behaviour of flames propagating from the closed end toward the open end of smooth horizontal tubes, in: J. de Physique IV (Proc.), Vol. 12, EDP sciences, 2002, pp. 265–271.

[54] C.-H. Tsai, The asymmetric behavior of steady laminar flame propagation in ducts, Combust. Sci. Technol. 180 (3) (2008) 533–545.

[55] D. Fernández-Galisteo, C. Jiménez, M. Sánchez-Sanz, V. N. Kurdyumov, The differential diffusion effect of the intermediate species on the stability of premixed flames propagating in microchannels, Combust. Theory Model. 18 (4-5) (2014) 582–605.

[56] V. N. Kurdyumov, Lewis number effect on the propagation of premixed flames in narrow adiabatic channels: Symmetric and non-symmetric flames and their linear stability analysis, Combust. Flame 158 (7) (2011) 1307–1317.

[57] V. N. Kurdyumov, C. Jiménez, Propagation of symmetric and non-symmetric premixed flames in narrow channels: Influence of conductive heat-losses, Combustion and Flame 161 (4) (2014) 927–936.

[58] G. Pizza, J. Mantzaras, C. E. Frouzakis, Flame dynamics in catalytic and non-catalytic mesoscale microreactors, Catalysis Today 155 (1) (2010) 123–130.

[59] J. Wan, A. Fan, Y. Liu, H. Yao, W. Liu, X. Gou, D. Zhao, Experimental investigation and numerical analysis on flame stabilization of ch 4/air mixture in a mesoscale channel with wall cavities, Combust. Flame 162 (4) (2015) 1035–1045.

List of Figures

Tables

Case	ϕ	$Y_{CH_4}\|_{inlet}$	$Y_{O_2}\|_{inlet}$	$Y_{N_2}\|_{inlet}$	$(u_x)\|_{inlet}[m \cdot s^{-1}]$	$T_{inlet}[K]$	R_e	$P[atm]$
a	0.37	0.021	0.228	0.751	1	750	186	1
b	0.37	0.021	0.228	0.751	2	729	390	1
c	0.31	0.018	0.229	0.753	1	754	186	1

Table 1: Inlet conditions for each case. ϕ, $(U_x)\|_{inlet}$ and T_{inlet} respectively stand for the equivalence ratio, axial velocity and temperature of the incoming mixture. $Y_{CH_4}\|_{inlet}$, $Y_{O_2}\|_{inlet}$ and $Y_{N_2}\|_{inlet}$ respectively refer to the CH_4, O_2 and N_2 species mass fractions at the inlet. R_e denotes the inlet Reynolds number based on the inlet velocity and channel height (H).

Boundary	Numerical condition	Imposed scalars or fluxes
Inlet	Inlet NSBC [43, 44]	Y_k, T and $\vec{u}$
Outlet	Outlet NSCBC [43, 44]	P
Catalytic wall	Reactive (Eqs. (11) to (13))	T, $\vec{u_w} \cdot \vec{n}$, $\vec{\nabla} Y_{k,w} \cdot \vec{n}$ and $q_w \cdot \vec{n}$
Plena walls	Adiabatic and free-slip	$\vec{u_w} \cdot \vec{n}$ and $\vec{q_w} \cdot \vec{n} = 0$
Channel centerline	Symmetry	No imposition.

Table 2: Type of boundary conditions used for the present study with the corresponding imposed scalars or fluxes.

Phase	time range	limiting time step	nodes	Procs	CPU time	G cost	S cost
AI + Propagati	$t \leq 3\, t_{AI}$	$CFL \approx 1 \times 10^{-8}$	1.2×10^6	256	72 h	40%	20%
Stabilization	$3\, t_{AI} \leq t \leq 12\, t_{AI}$	$CFL \approx 1 \times 10^{-7}$	60.000	32	11 h	40%	10%

Table 3: CPU cost of the calculation under the conditions of case (a). G cost and S cost respectively stand for the CPU time consumed by gas-phase and surface chemistry. A similar cost is observed for case (b) and (c).

Case	x_{stab}^{exp}[mm]	x_{stab}^{num} [mm]	Relative difference (%)	$\dfrac{\|x_{stab}^{exp} - x_{stab}^{num}\|}{h_c}$
a	86.25	86.1	0.2	0.04
b	162.5	166.8	2.5	1.23
c	91.5	90.35	1	0.33

Table 4: Comparison of the predicted stabilization positions of the flames (x_{stab}^{num}) with the experimental value (x_{stab}^{exp}).

Case	Relative difference of maximum axial OH levels (%)	Relative difference of OH profile thickness (%)	$\dfrac{\|L_{OH}^{exp} - L_{OH}^{num}\|}{L_{OH}^{exp}}$
a	38	45	0.9
b	62	32	0.4
c	75	36	0.8

Table 5: Comparison of the predicted maximum OH levels and flame thickness with the experiment. L_{OH}^{exp} and L_{OH}^{num} respectively refer to the experimental and predicted values.

Case	$\dfrac{x_{stab} - x_{stab}^{ref}}{L_c}$ (%)	$\dfrac{x_{stab} - x_{stab}^{ref}}{h_c}$ (%)
OS	-4	-314
OF	+1.2	+17
CS	-0.8	-57
CF	+2.4	+86

Table 6: Comparison of the predicted stabilization positions of the flames for the catalytic channels with obstacles and cavities. x_{stab} is the axial distance between the inlet of the catalytic channel and the axial point where the OH concentration reaches its maximum. x_{stab}^{ref} refers to the planar wall case (a).

Figures
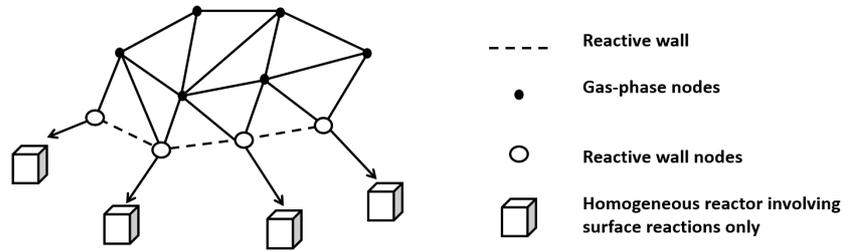
Figure 1: Sketch of the surface kinetics numerical resolution.
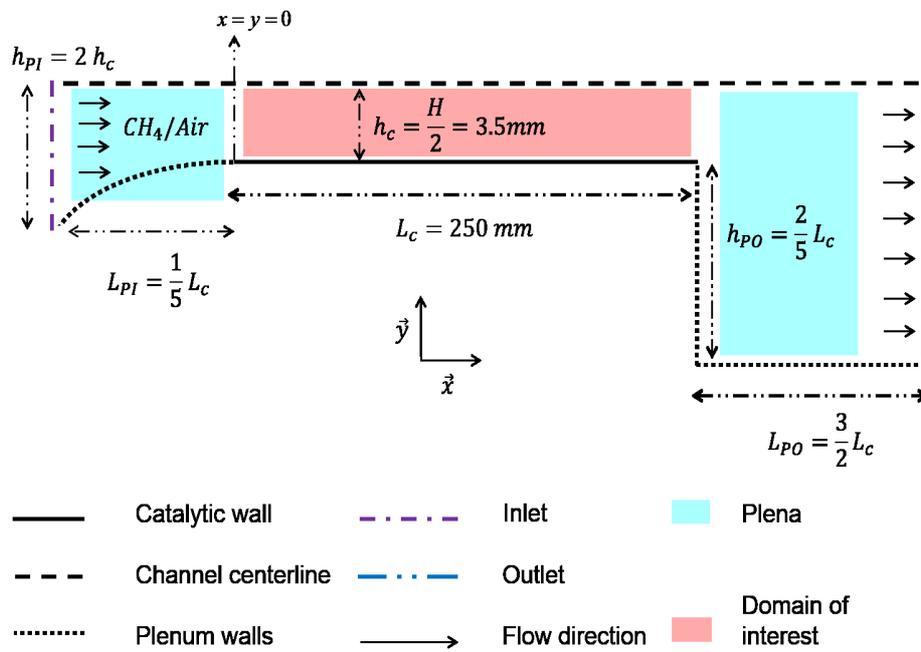
Figure 2: Computational domain of the catalytic channel (domain of interest). Up- and downstream plena are added for the numerical imposition of I/O boundary conditions.
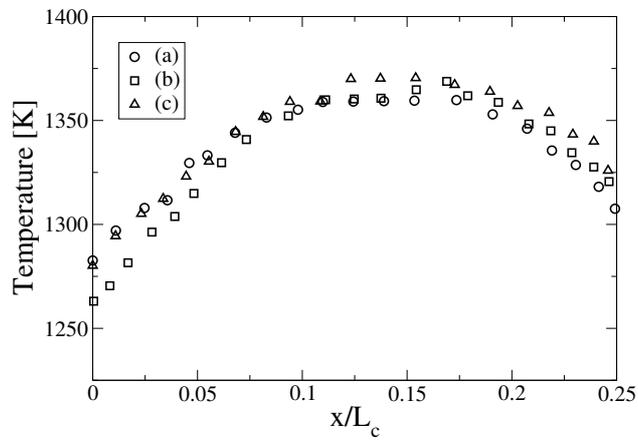
Figure 3: Experimental wall temperature profiles prescribed at the catalytic wall.
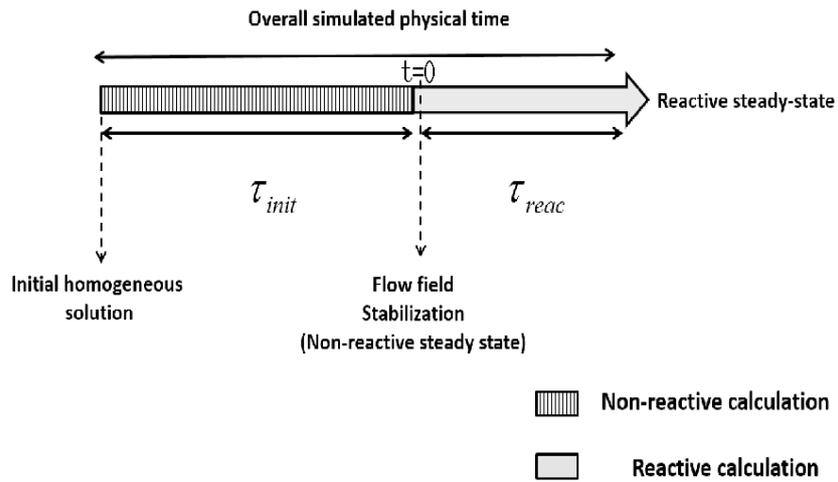
Figure 4: Illustration of the calculation methodology.
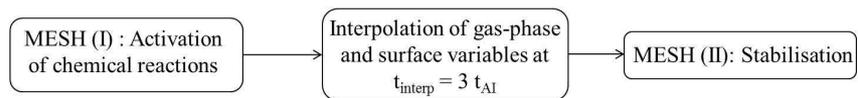
Figure 5: Summary of the meshing strategy, t_{interp} and t_{AI} respectively stand for the interpolation time and the physical time at which chemical reactions are activated.

(a) Measurement

(b) Simulation
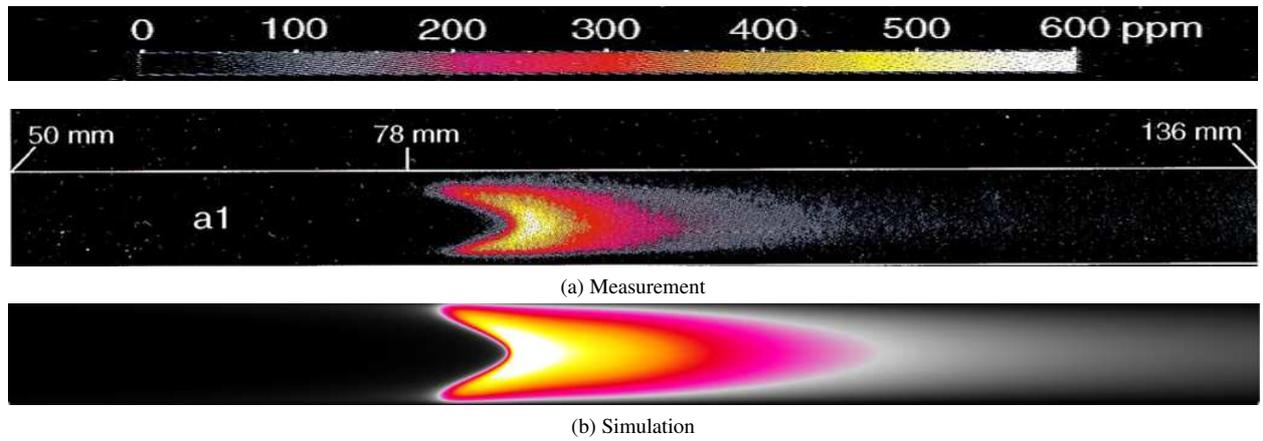
Figure 6: 2D *OH* concentration maps for case (a).

(a) Measurement

(b) Simulation
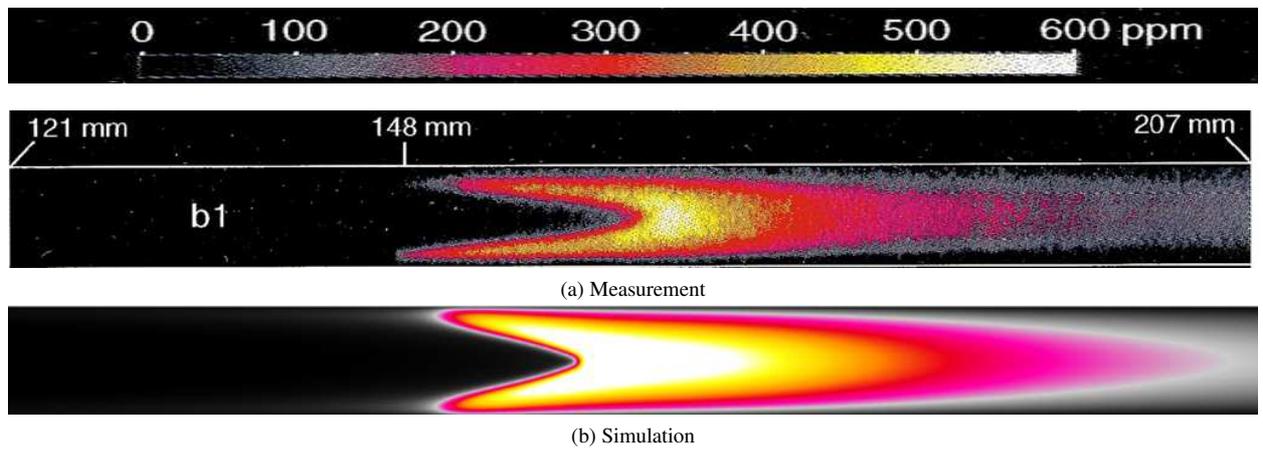
Figure 7: 2D *OH* concentration maps for case (b).

(a) Measurement

(b) Simulation
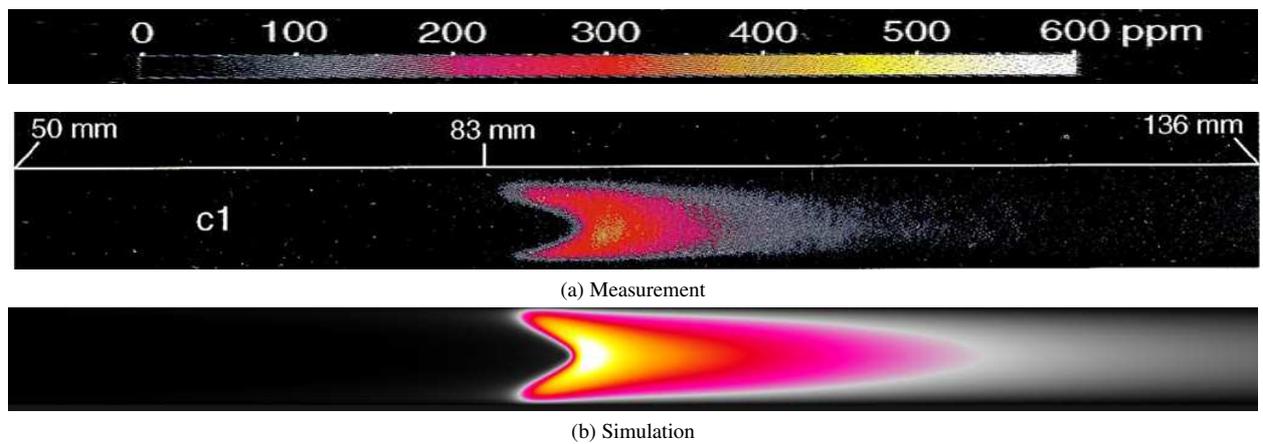
Figure 8: 2D *OH* concentration maps for case (c).

23
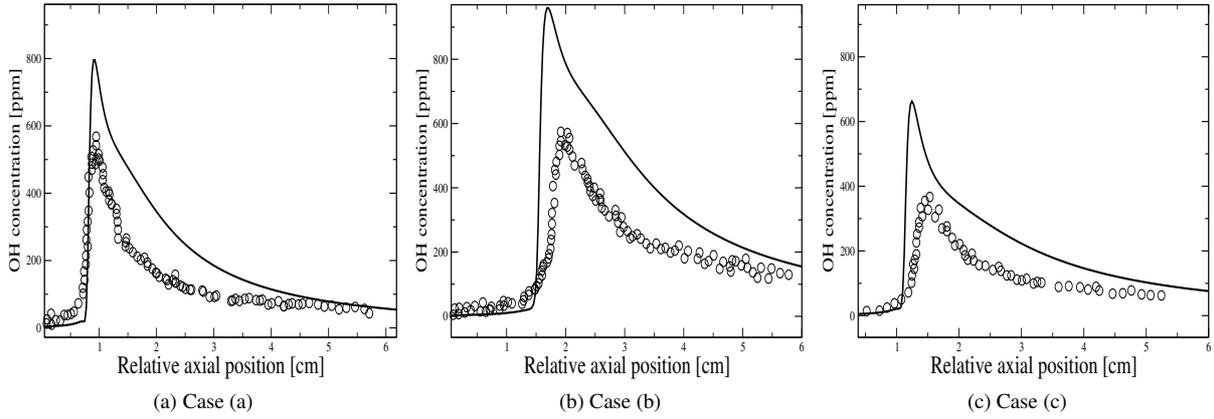
Figure 9: Comparison of axial OH profiles along the channel plane of symmetry for cases (a, b, c). Symbols : Experiments. Lines : Calculations.

(a) $\tau = t/t_{AI} = 1.5$

(b) $\tau = t/t_{AI} = 1.65$
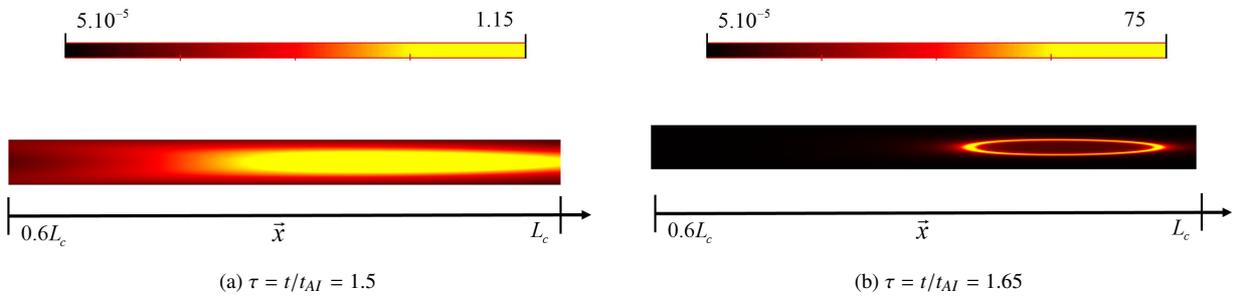
Figure 10: 2D Normalized gas-phase heat release rate $\dfrac{\dot{\omega}_T}{\dot{\omega}_T^{0D}}$ at two instants during the ignition phase for case (a).

(a) Normalized OH mass fraction

(b) Normalized gas-phase heat release rate
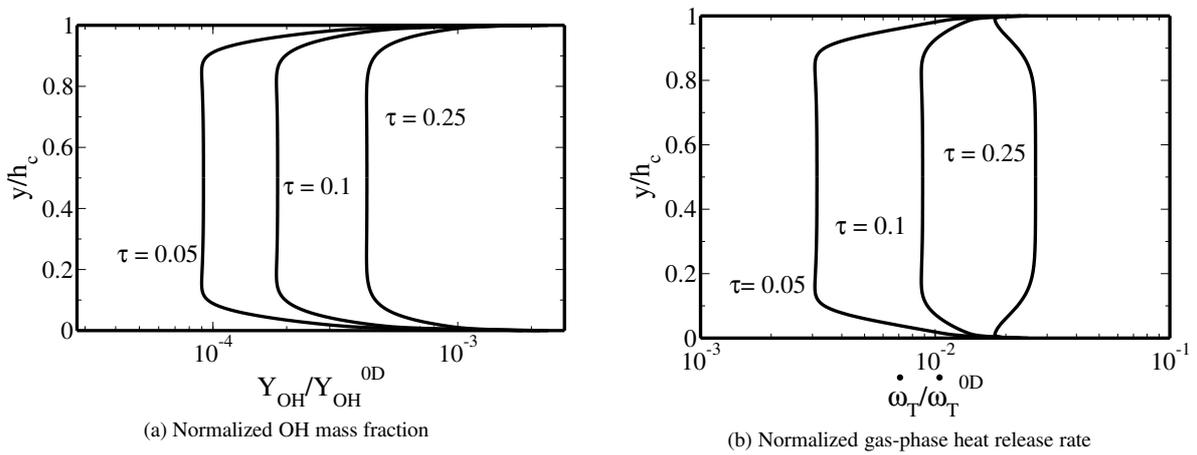
Figure 11: Transverse profiles (Log scale) at $x = 0.9\,L_c$ for different instants $\tau = t/t_{AI}$ and case (a).

24

(a) Normalized OH mass fraction (Log scale)

(b) Normalized gas-phase heat release(Log scale)
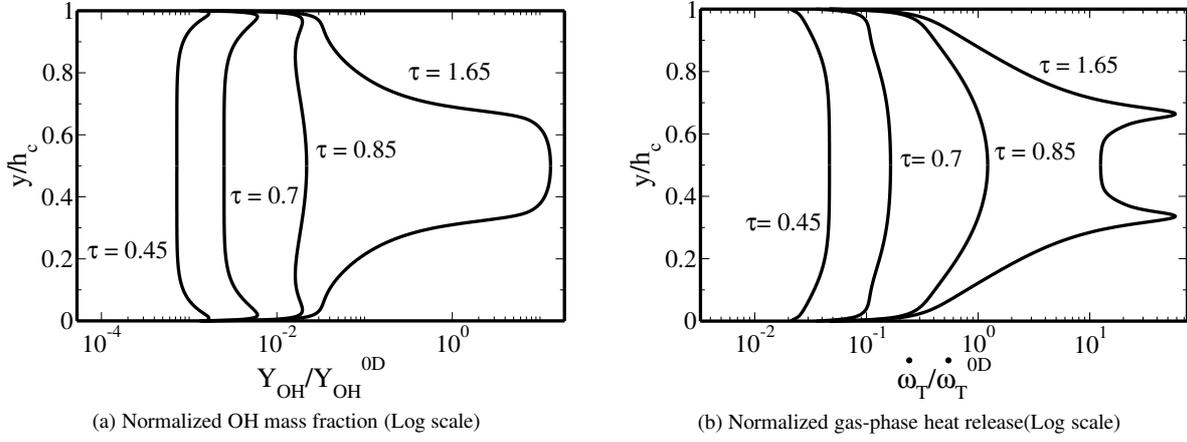
Figure 12: Transverse profiles (Log scale) at $x = 0.9\,L_c$ for different instants $\tau = t/t_{AI}$ and case (a).
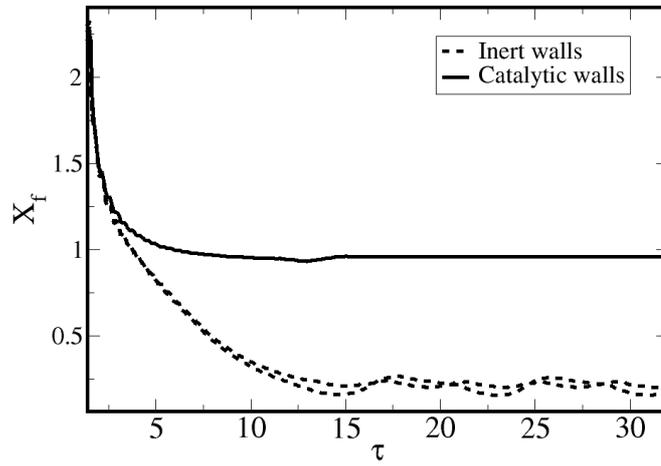
Figure 13: Temporal evolution of the normalized reaction front position X_f taken at $y = 0.5h_c$ and $1.5h_c$: Channel with inert walls versus catalytic channel. τ is the normalized time $\tau = t/t_{AI}$.

(a) Channel with reactive walls: $t = 25\,t_{AI}$

(b) Channel with inert walls: $t = 23\,t_{AI}$

(c) Channel with inert walls: $t = 26\,t_{AI}$
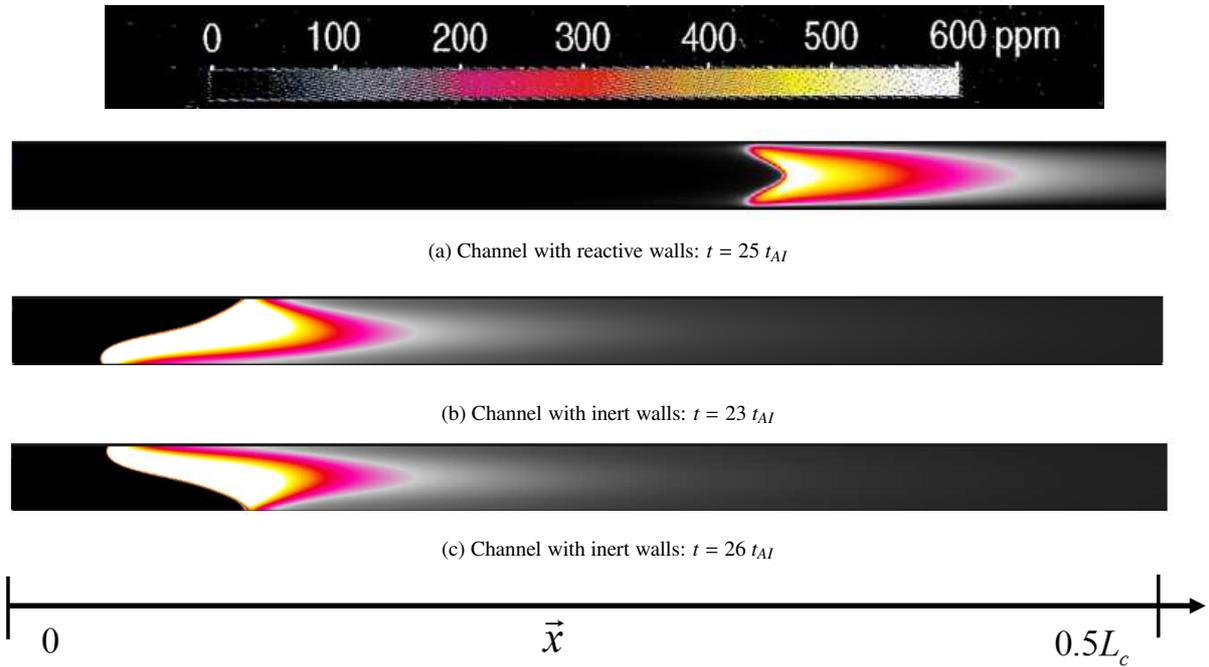
Figure 14: *OH* concentration maps for the channel with inert walls.

(a) with obstacles

(b) with cavities
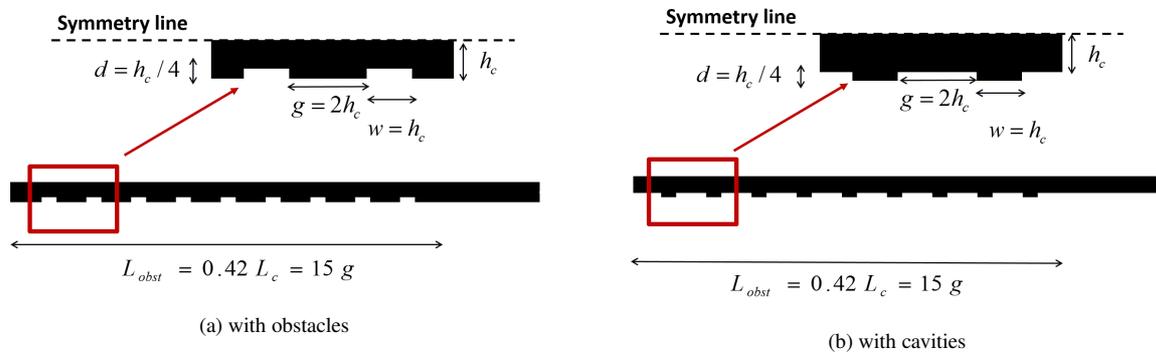
Figure 15: Schematic of the catalyst channels.

Figure 16: Reduction and increase of the planar-walls channel section by the respective introduction of obstacles and cavities. Middle : planar-wall channel, left: obstacles, right: cavities.

(a) Full *Pt*-coating (OF case)

(b) Segmented *Pt*-coating (OS case)

(c) Full *Pt*-coating (CF case)

(d) Segmented *Pt*-coating (CS case)
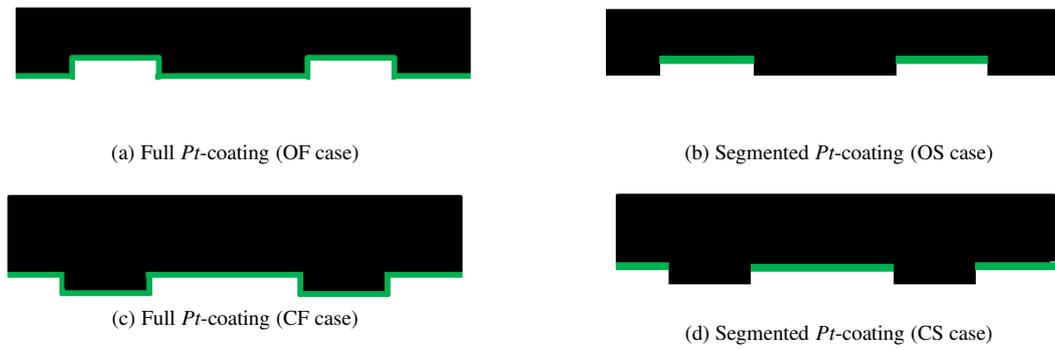
Figure 17: *Pt*-coatings considered for the channel with obstacles (top) and cavities (bottom): the green segments highlight the edges covered with *Pt*.
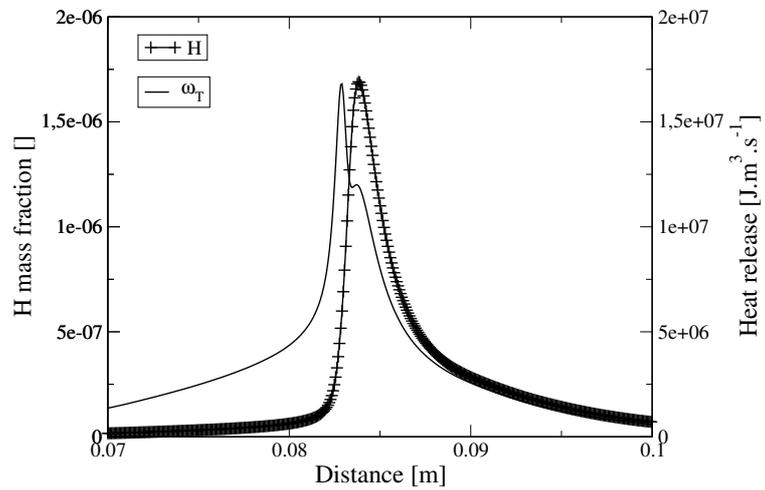
Figure 18: Spatial resolution of H species within the reaction zone along the channel plane of symmetry (OS case).The heat release profile is also plotted.
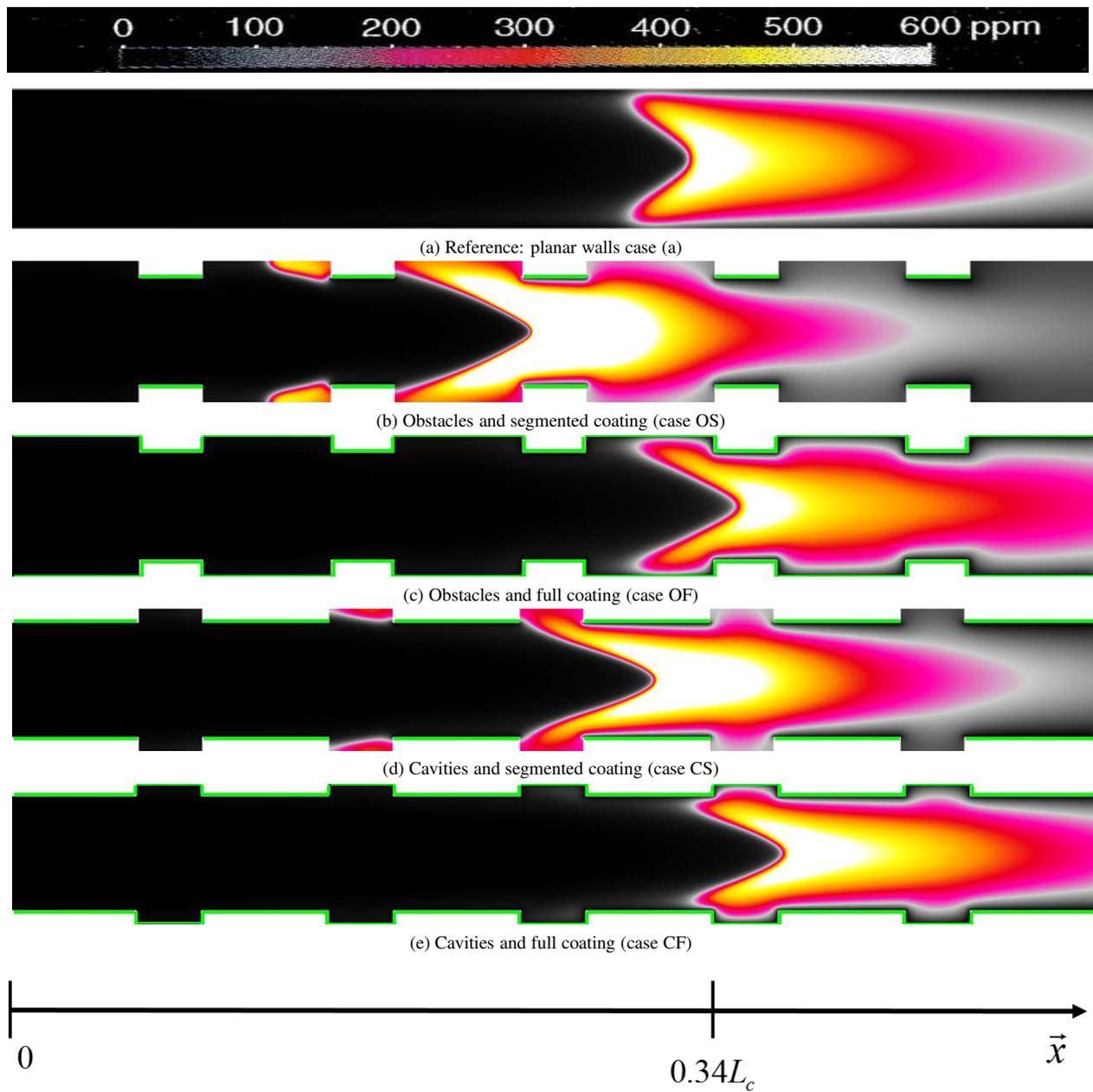
0   100   200   300   400   500   600 ppm

(a) Reference: planar walls case (a)

(b) Obstacles and segmented coating (case OS)

(c) Obstacles and full coating (case OF)

(d) Cavities and segmented coating (case CS)

(e) Cavities and full coating (case CF)

0 $0.34L_c$ $\vec{x}$

Figure 19: Comparison of the *OH* concentration maps: Effect of obstacles, cavities and coating type on the anchoring position. Catalytic walls are marked with green lines.

28
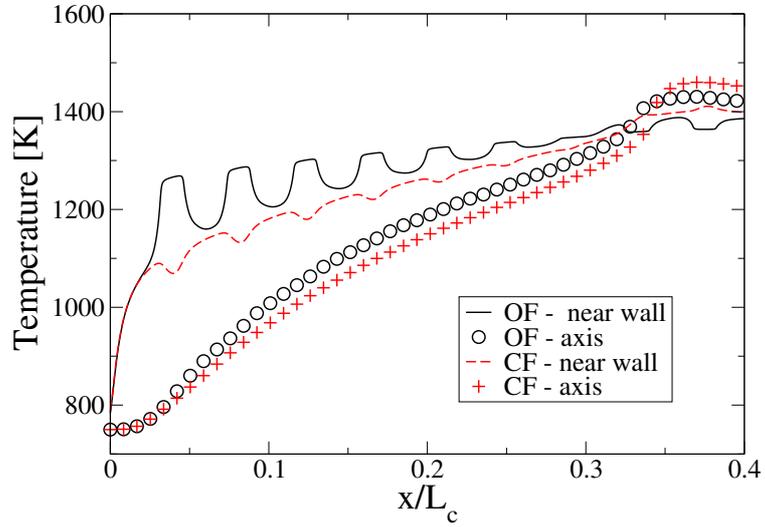
Figure 20: Longitudinal profiles of the temperature along the channel plane of symmetry and 1 mm above the catalytic wall for cases OF and CF.

(a)

(b)
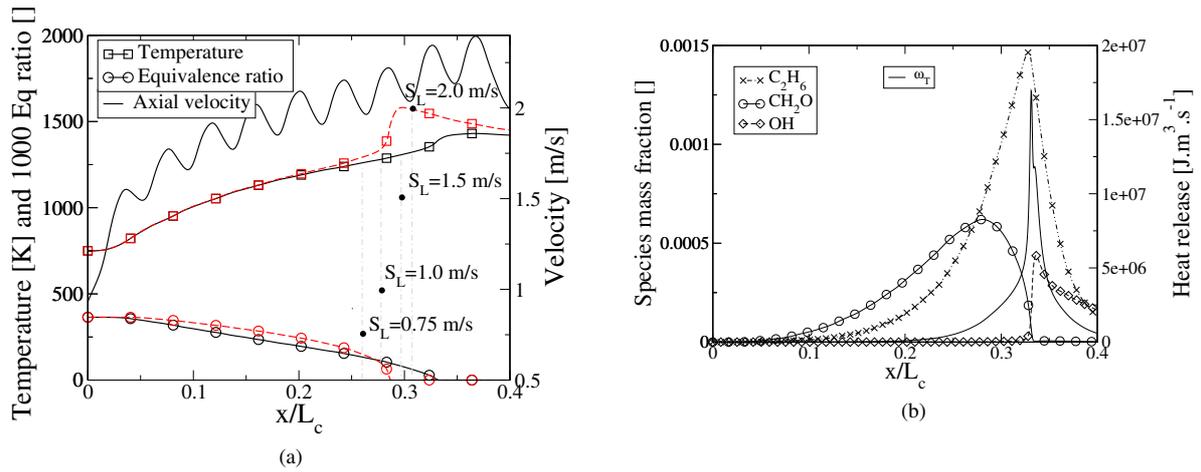
Figure 21: Longitudinal profiles along the channel center line, (a) gas velocity, temperature and equivalence ratio for cases OF (solid lines) and OS (red dashed lines); (b) gaseous heat release rate and species mass fractions for case OF.
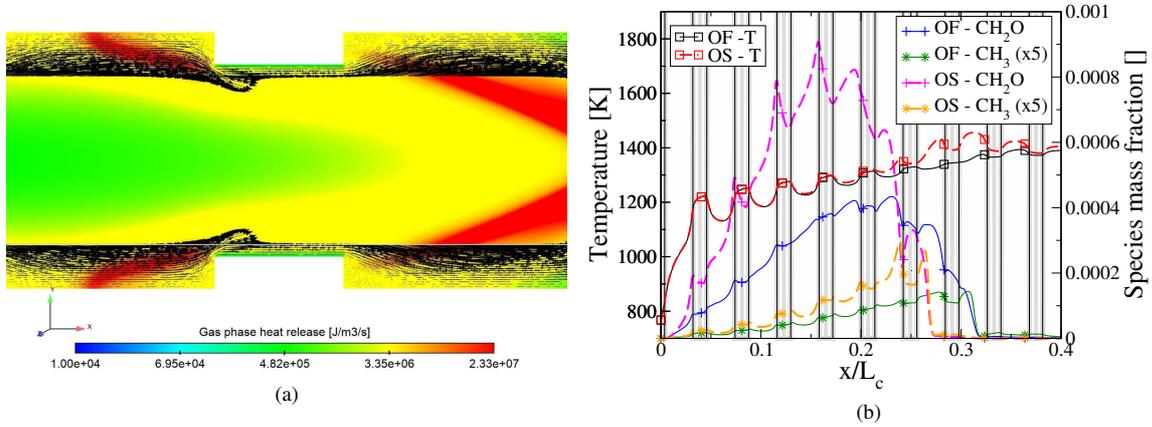
(a)

(b)

Figure 22: Spatial field and near-wall longitudinal profiles with obstacles, (a) gaseous heat release rate (log scale) and velocity vectors (up to 1mm above the catalytic wall) for cases OS; (b) longitudinal profiles of temperature and species 1mm above the catalytic wall for cases OF (solid lines) and OS (dashed lines).
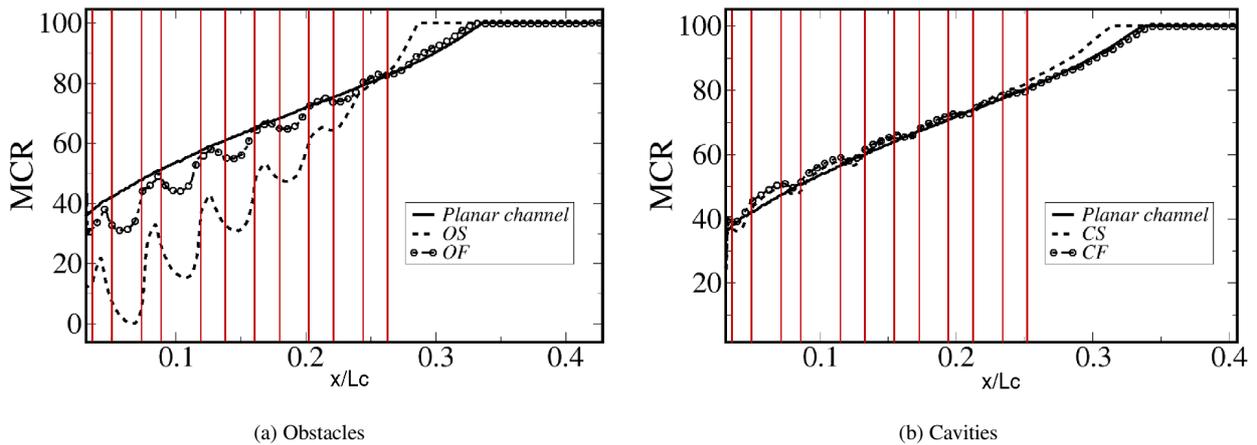

(a) Obstacles

(b) Cavities

Figure 23: Methane conversion for both types of Pt-coating : obstacles $vs.$ cavities.
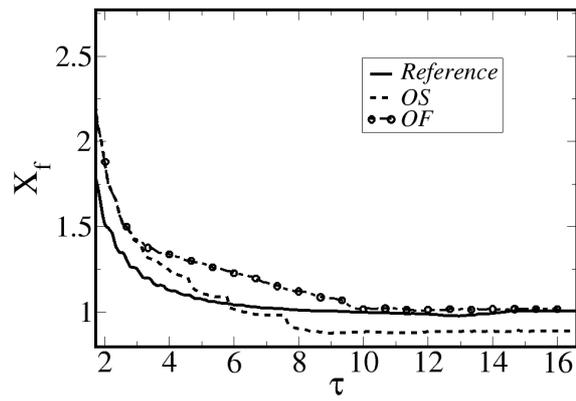
Figure 24: Temporal evolution of the normalized flame front positions X_f for the channels with obstacles.

(a) $\tau = 7$

(b) $\tau = 7.2$
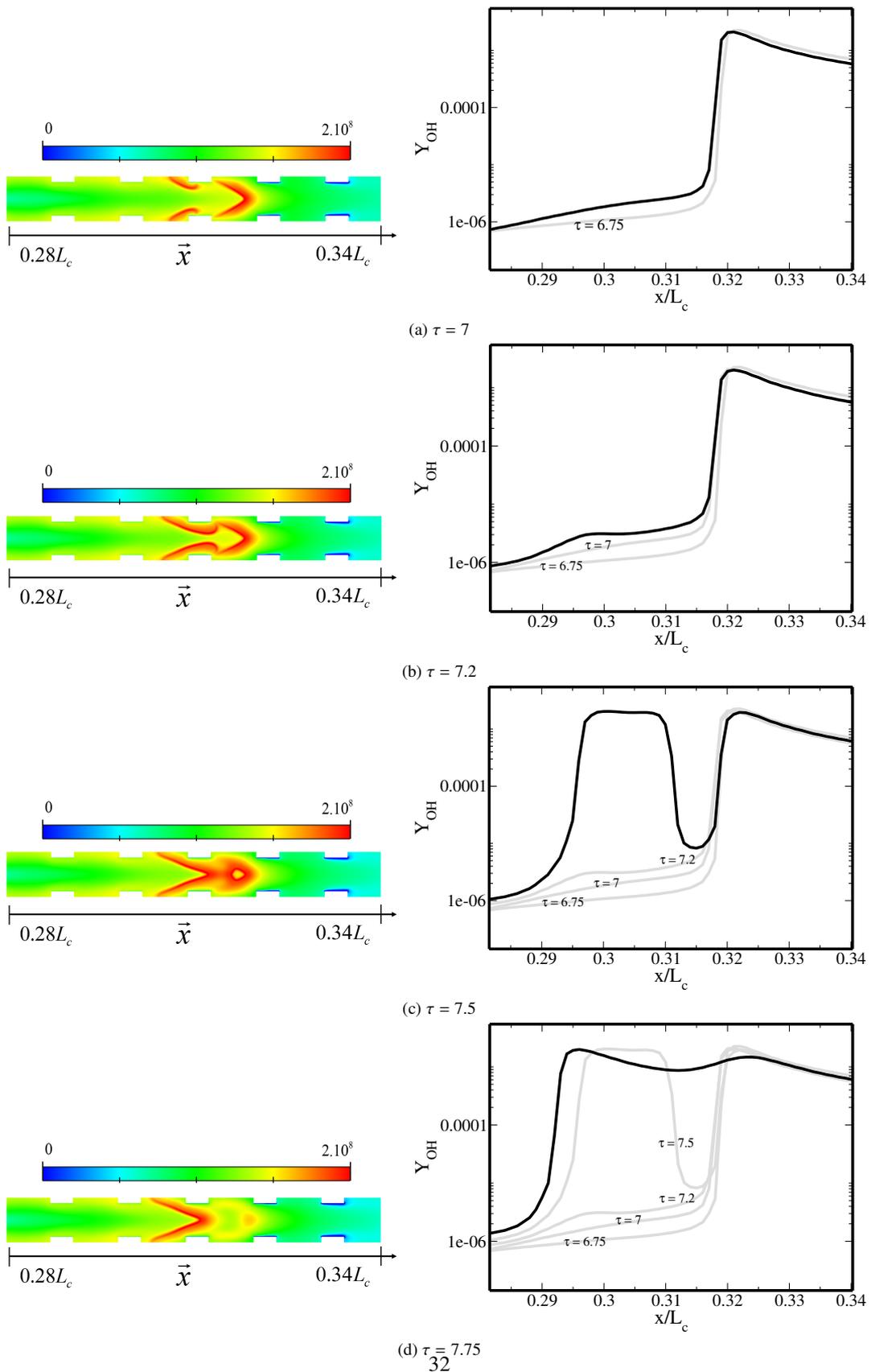
(c) $\tau = 7.5$

(d) $\tau = 7.75$

Figure 25: Propagation dynamics for the OS case. Left : gas-phase heat release rate (log scale); right: Y_{OH} channel profile along the plane of symmetry. The grey OH lines stand for the past whereas the thick black lines refer to the present profiles.
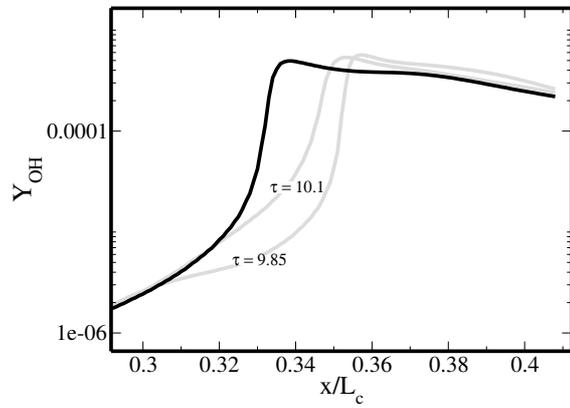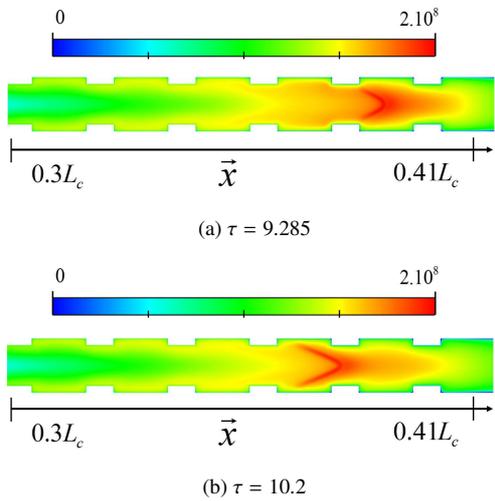
(a) $\tau = 9.285$

(b) $\tau = 10.2$

(c)

Figure 26: Propagation dynamics for the OF case. Left : gas phase heat release (log scale); right : OH mass fraction profile along the plane of symmetry.